bioRxiv preprint doi: https://doi.org/10.1101/638296; this version posted May 14, 2019. The copyright holder for this preprint (which was not certified by peer review) is the author/funder. All rights reserved. No reuse allowed without permission.

Septin 2/6/7 complexes tune microtubule plus end growth and EB1 binding in a concentration-dependent manner

Konstantinos Nakos[a], Megan R. Radler[a] and Elias T. Spiliotis[a,*]

[a]Department of Biology, Drexel University, Philadelphia, PA 19104

*Address correspondence to Elias Spiliotis (ets33@drexel.edu)

Keywords: microtubule plus ends; microtubule plus end tips; microtubule catastrophe; pause; septins; septin filaments; EB1 inhibition

Abbreviations used: MT, microtubules; SEPT2/6/7, Septin 2/6/7 complex; SEPT9, Septin 9; SEPT5, Septin 5; EB1, End-Binding protein 1; GMPCPP, guanosine-5'-[(α,β)-methyleno]triphosphate; GTPγS, guanosine 5'-O-[gamma-thio]triphosphate; GDP, guanosine diphosphate; GTP, Guanosine-5'-triphosphate; TIRF, total internal reflection fluorescence

bioRxiv preprint doi: https://doi.org/10.1101/638296; this version posted May 14, 2019. The copyright holder for this preprint (which was not certified by peer review) is the author/funder. All rights reserved. No reuse allowed without permission.

Abstract

Septins are filamentous GTP-binding proteins, which affect microtubule-dependent functions including membrane trafficking and cell division, but their precise role in microtubule dynamics is poorly understood. Here, in vitro reconstitution of microtubule dynamics with SEPT2/6/7 complexes, the minimal subunits of septin heteromers, shows that SEPT2/6/7 stabilizes and pauses microtubule plus ends in their growth phase, and inhibits tracking of the microtubule plus end protein EB1 in a concentration-dependent manner. We show that SEPT2/6/7 competes with EB1 for binding to GTPγS-stabilized microtubules, which mimic the EB1-preferred GDP-Pi state of polymerized tubulin. On dynamic microtubules, however, SEPT2/6/7 rarely binds microtubule plus ends, suggesting that SEPT2/6/7 impacts EB1-binding allosterically through long-range effects on the GDP-bound lattice. Strikingly, plus end pausing and EB1 dissociation also occur during end-on collisions of microtubules with immobilized SEPT2/6/7 filaments, which have a greater impact than actin filaments. In agreement with these in vitro findings, EB1 pausing is enhanced upon contact with septins in primary hippocampal neurons. Taken together, these data demonstrate that SEPT2/6/7 complexes and filaments can directly tune microtubule plus end dynamics and the tracking of plus end proteins, providing a mechanism for capture and guidance of MT plus ends at intracellular regions of septin localization.

bioRxiv preprint doi: https://doi.org/10.1101/638296; this version posted May 14, 2019. The copyright holder for this preprint (which was not certified by peer review) is the author/funder. All rights reserved. No reuse allowed without permission.

Introduction

Septins are GTP-binding proteins that assemble into filamentous higher-order oligomers and polymers comprising a major component of the mammalian cytoskeleton along actin, microtubules and intermediate filaments (Spiliotis, 2018). Septins associate with microtubules (MTs) and affect MT organization and dynamics in various cell types (Ageta-Ishihara et al., 2013; Bai et al., 2013; Bowen et al., 2011; Kremer et al., 2005). Notably, septins are functionally involved in MT-dependent functions such as cell division and polarized membrane traffic (Estey et al., 2010; Karasmanis et al., 2018; Menon et al., 2014; Spiliotis et al., 2008; Spiliotis et al., 2005). A growing number of studies suggests that septins are involved in the entry and growth of MTs in membrane protrusions (e.g., filopodia, cilia, micro-tentacles) (Ghossoub et al., 2013; Nolke et al., 2016; Ostevold et al., 2017), but how septins affect the dynamic instability of MTs is not well understood.

Mammalian septins are a family of 13 paralogous genes, which are classified in four groups named after SEPT2, SEPT3, SEPT6 and SEPT7 (Kinoshita, 2003b; Russell and Hall, 2011; Weirich et al., 2008). The minimal building block of septin heteromers is a palindromic hetero-hexamer that contains septins from the SEPT2, SEPT6 and SEPT7 groups in a stoichiometry of 2:2:2 (Sirajuddin et al., 2007). Septins which can become a hetero-octamer with SEPT9 (SEPT3 group) capping the ends of the SEPT7-SEPT6-SEPT2-SEPT2-SEPT6-SEPT7 complex (Kim et al., 2011; Kinoshita, 2003a; Sellin et al., 2011; Sheffield et al., 2003). Depending on the relative expression of septin paralogs, which differs among cell types, individual subunits of septin heteromers colocalize with MTs (Sellin et al., 2012, 2014; Silverman-Gavrila and Silverman-Gavrila, 2008; Spiliotis et al., 2008; Spiliotis et al., 2005; Targa et al., 2019). MT-associated septins have the appearance of filaments, but it is unclear whether they decorate the MT lattice as oligomers or assemble into higher-order filaments along the MT surface. It is also not well understood whether every septin subunit interacts with MTs. SEPT9 binds MTs directly through N-terminal repeat motifs (K/R-R/x-x-D/E), which associate with the C-terminal tails of β-

bioRxiv preprint doi: https://doi.org/10.1101/638296; this version posted May 14, 2019. The copyright holder for this preprint (which was not certified by peer review) is the author/funder. All rights reserved. No reuse allowed without permission.

tubulin (Bai et al., 2013). It is unclear whether these motifs function in septins of the SEPT6 and SEPT7 groups, which also associate with MTs, but SEPT2 does not appear to bind MTs directly (Bai et al., 2013).

How septins, as individual subunits or heteromeric complexes, impact the dynamic properties of MTs has been difficult to determine owing to disparate results in septin-depleted cells. SEPT7 was initially posited to enhance MT dynamics, because SEPT7 knock-down increased MT acetylation, a marker of MT stability (Janke and Montagnac, 2017; Kremer et al., 2005). However, this effect was attributed to cytosolic SEPT7, which sequestered the microtubule-associated protein 4 (MAP4) away from MTs (Kremer et al., 2005) and promoted the interaction of histone deacetylase HDAC6 with cytosolic free tubulin (Ageta-Ishihara et al., 2013). Comprehensive analysis of MT dynamics in SEPT2-depleted MDCK cells revealed a distinct increase in MT catastrophe, indicating that septins promote persistent MT growth and thereby, may promote MT growth. Additionally, SEPT2 knock-down decreased MT growth and turning at MT-MT intersections, suggesting that MT-associated septins may guide the directionality of MT growth (Bowen et al., 2011). In support of this possibility, septins were proposed to promote the formation of MT-driven membrane protrusions through an interplay with the MT plus end tracking protein EB1 in cells that are infected with *C. difficle* transferase (Nolke et al., 2016). Despite these findings, the underlying mechanism(s) by which septins impact MT dynamics remain elusive.

To better understand how the dynamic instability of MTs is modulated by septins, we have used total internal reflection fluorescence (TIRF) microscopy to assay MT dynamics in the presence of recombinant SEPT2/6/7 as the minimal subunits of septin heteromers. We have found that SEPT2/6/7 complexes exert concentration-dependent effects on MT plus end dynamics and the MT plus end tracking protein EB1, which may provide a novel mechanism for the capture and guidance of MT plus ends at cytoskeletal and membrane domains of septin enrichment.

bioRxiv preprint doi: https://doi.org/10.1101/638296; this version posted May 14, 2019. The copyright holder for this preprint (which was not certified by peer review) is the author/funder. All rights reserved. No reuse allowed without permission.

Results

SEPT2/6/7 tunes MT plus end dynamics in a concentration- and assembly state-dependent manner

Using a TIRF microscopy assay that visualizes the polymerization and depolymerization of Rhodamine-labeled tubulin onto stable HiLyte 488-labeld MT seeds, we tested how MT dynamics is impacted by different concentrations of recombinant SEPT2/6/7 complexes, which were purified from bacteria (Figure S1). Quantification of the parameters of MT dynamics revealed a biphasic concentration-dependent response for catastrophe frequencies and MT lengths (Figure 1c,d). Lower concentrations of SEPT2/6/7 (10 - 400 nM) reduced catastrophe frequencies by 20-34% and increased MT lengths by 1.2-to-1.8-fold, whereas higher concentrations of SEPT2/6/7 (>1 μM) had the opposite effect, enhancing catastrophe frequencies by 1.2-to-1.6-fold and decreasing MT lengths by 30-48%. A similar, but less pronounced, biphasic effect was observed for the rates of MT growth, which increased slightly at 10 nM of SEPT2/6/7 and decreased gradually at concentrations >800 nM, while no effect was observed between 10 and 800 nM (Figure 1a). Interestingly, the rates of MT depolymerization were not affected in a biphasic manner, but rather decreased steadily with increasing concentrations of SEPT2/6/7 (Figure 1b). As also evidenced by the kymographs of MT dynamics (Figure 1e-m), these data show that lower concentrations of SEPT2/6/7 (<0.5 μM) induce persistent MT growth by decreasing the frequency of catastrophe events and rates of depolymerization. Micromolar concentrations of SEPT2/6/7 (>1 μM), however, dampen MT dynamics and reduce MT lengths by decreasing rates of MT growth and enhancing catastrophe.

Because SEPT2/6/7 complexes assemble into higher-order filamentous structures, which depend on concentration and ionic conditions, we reasoned that the biphasic effect might be due to concentration-dependent differences in the assembly state of SEPT2/6/7 complexes. To assess the higher-order state of SEPT2/6/7, we performed a sedimentation assay after diluting and incubating SEPT2/6/7 complexes in the buffer of the MT dynamics assay. Quantifications of

bioRxiv preprint doi: https://doi.org/10.1101/638296; this version posted May 14, 2019. The copyright holder for this preprint (which was not certified by peer review) is the author/funder. All rights reserved. No reuse allowed without permission.

SEPT2/6/7 in the pellet and supernatant fractions showed that the levels of sedimenting higher-order septins were fairly equivalent up to concentrations of 400 nM, but increased in a stepwise concentration-dependent manner above 800 nM (Figure S1a,b). This increase in the amount of higher-order SEPT2/6/7 correlated with the dampening of MT dynamics observed at concentrations >800 nM (Figure 1a, c-d). Hence, SEPT2/6/7 filaments do not appear to favor MT growth and elongation, which is enhanced by lower concentrations of SEPT2/6/7 (Figure 1).

Given that MT growth and dynamics are inhibited by higher concentrations of SEPT2/6/7 (>800 nM), we asked whether higher-order SEPT2/6/7 complexes associate with free unpolymerized tubulin, lowering the effective concentration of tubulin that is available to polymerize. This is plausible as we recently found that SEPT9 binds and recruits free tubulin to the MT lattice (Nakos et al., 2019). To test this possibility, SEPT2/6/7 and SEPT9 complexes were immobilized on functionalized glass chambers and fluorescent tubulin was added in the buffer conditions of the MT dynamics assay (Figure S2a). Binding of soluble tubulin to septin complexes was visualized by TIRF imaging similar to a previous assays of MT nucleation (Lazarus et al., 2013). While tubulin was increasingly bound to chambers with sub-micromolar concentrations of SEPT9, no binding was observed for a similar concentration range of SEPT2/6/7 (Figure S2b,c). These data indicate that SEPT2/6/7 does not sequester unpolymerized tubulin and the effects of SEPT2/6/7 on MT dynamics depend on the septin concentration and assembly state (oligomers vs. higher order polymers).

SEPT2/6/7 pauses MT plus end growth

In kymographs of MT dynamics, we noticed that MT plus ends exhibited a variety of pausing events in the presence of SEPT2/6/7 complexes. In several kymographs, MT plus ends paused transiently while growing and subsequently, depolymerized or continued to grow before undergoing catastrophe (Figure 2b,d, arrow heads). Although much less frequent, MT plus ends also paused transiently during catastrophe before depolymerizing to the MT seed (Figure 2c,d).

bioRxiv preprint doi: https://doi.org/10.1101/638296; this version posted May 14, 2019. The copyright holder for this preprint (which was not certified by peer review) is the author/funder. All rights reserved. No reuse allowed without permission.

Additionally, the slope of depolymerization events was shallower, which was consistent with decreased rates of depolymerization (Figure 1).

Given the concentration dependence of SEPT2/6/7 effects on MT dynamics, we analyzed the frequency of pausing events that occurred in growth phases. Strikingly, MT pausing increased with increasing concentrations of SEPT2/6/7 peaking at 400 nM, where the percentage of MTs with pausing events doubled (23.2% to 48.5%) (Figure 2e). This pausing effect was unique to SEPT2/6/7 as SEPT9 did not cause a similar effect (Figure 2f). However, at concentrations of SEPT2/6/7 over 400 nM, MT pausing began to decrease and micromolar concentrations of SEPT2/6/7 did not increase pausing above the levels observed in the absence of SEPT2/6/7. Hence, MT pausing appears to be an intermediate phenotype that occurs by SEPT2/6/7 complexes in between concentrations that promote and inhibit MT growth and elongation.

SEPT2/6/7 associates with the MT lattice and plus ends

Based on the effects of SEPT2/6/7 on MT plus end growth and pausing, we sought to examine whether SEPT2/6/7 complexes associate with the lattice and/or tips of dynamic MT plus ends. TIRF imaging of mCherry-SEPT2/6/7 showed a concentration-dependent association with the lattice of MT seeds and polymerized plus ends. At concentrations lower than 200-400 nM, mCherry-SEPT2/6/7 localized sparsely and in patches on the lattice of MT seeds and plus end segments (Figure 3a). Because of the sparse localization, we quantified MTs categorically based on the distribution of mCherry-SEPT2/6/7 puncta (Figure 3b). We found that the majority of MTs contained mCherry-SEPT2/6/7 at either MT seeds or the lattice segments of MT plus ends in equal frequency (~30% of total MTs each). A significant percentage contained mCherry-SEPT2/6/7 on both seed and plus end segments (11.5%) as well as on the seed and plus end tips (11.5%). In kymographs of time-lapse imaging, we observed binding of mCherry-SEPT2/6/7 to the lattice of MT plus ends, which persisted for several seconds to a few minutes, and occasional associations with growing and depolymerizing plus end tips (Figure 3a, c). At

bioRxiv preprint doi: https://doi.org/10.1101/638296; this version posted May 14, 2019. The copyright holder for this preprint (which was not certified by peer review) is the author/funder. All rights reserved. No reuse allowed without permission.

concentrations >100 nM, mCherry-SEPT2/6/7 associated with MTs more extensively (Figure 3d,e). Quantification of mCherry-SEPT2/6/7 fluorescence on the lattice of MT seeds vs. plus ends showed a modest preference (~1.5-fold difference) for the GMPCPP-stabilized lattice (Figure 3f,g), which quantitatively was much milder than the ~4-fold difference that was previously observed for SEPT9, which in similar concentrations (400-800 nM) did not fully decorate the lattice of MT plus ends (Nakos et al., 2019). Hence, SEPT2/6/7 appears to have a higher affinity than SEPT9 for the lattice of MT plus end segments, which correlates with the pausing effects of SEPT2/6/7 on plus ends, an effect that is not observed with SEPT9.

SEPT2/6/7 complexes inhibit MT plus end binding and tracking of EB1

Recent reports of an interaction between EB1 and septins (Nolke et al., 2016) raises the question whether EB1 and SEPT2/6/7 cooperate or compete with one another on MT plus ends. Given the effects of SEPT2/6/7 on MT plus ends, we sought to test whether SEPT2/6/7 affects the binding and dynamics of the plus end-binding protein EB1, which can also provide more insight into how SEPT2/6/7 impacts MT plus end dynamics.

We reconstituted MT dynamics in the presence of recombinant EB1-GFP and mCherry-SEPT2/6/7 (Figure 4a). Tracking of EB1-GFP on MT plus ends required buffer conditions (50 mM KCl), which limit diffusive interactions of EB1-GFP with the MT lattice (Zanic et al., 2009). In these ionic conditions, the MT-binding affinity of mCherry-SEPT2/6/7 was reduced, but mCherry-SEPT2/6/7 exhibited the same concentration-dependent pattern of decoration with a modest preference for the GMPCPP-bound MT seeds.

In the absence of mCherry-SEPT2/6/7, EB1-GFP (75 nM) tracked on growing MT plus ends and was absent from MT tips during catastrophe (Bieling et al., 2008; Bieling et al., 2007; Dixit et al., 2009). In kymographs, EB1-GFP appeared as diagonal lines, outlining the trajectory of the growing MT plus ends (Figure 4a). Strikingly, the fluorescence intensity of EB1-GFP decreased with increasing concentrations of mCherry-SEPT2/6/7, which was indicative of a

bioRxiv preprint doi: https://doi.org/10.1101/638296; this version posted May 14, 2019. The copyright holder for this preprint (which was not certified by peer review) is the author/funder. All rights reserved. No reuse allowed without permission.

reduction in the binding of EB1-GFP to growing MT plus ends (Figure 4a). Quantification of EB1-GFP fluorescence showed a statistically significant reduction in the presence of 400 - 800 nM mCherry-SEPT2/6/7 (Figure 4b). Surprisingly, however, mCherry-SEPT2/6/7 did not localize or track on growing MT plus end tips. No co-localization or co-tracking with EB1-GFP was observed at low septin concentrations (<200 nM). Notably, mCherry-SEPT2/6/7 was also absent from MT plus end tips at higher concentrations, which caused the dissociation of EB1-GFP from MT plus ends.

Inhibition of EB1-GFP binding and tracking by SEPT2/6/7 pointed to a few possibilities. First, EB1-GFP might be sequestered by soluble SEPT2/6/7 complexes as has been shown before for tau (Ramirez-Rios et al., 2016). Second, SEPT2/6/7 may compete transiently with EB1 for binding to tips of MT plus ends that transition from tubulin-GTP to tubulin-GDP-Pi, which are respectively the low- and high-affinity binding sites of EB1 (Maurer et al., 2011; Maurer et al., 2012; Zanic et al., 2009). Third, binding of SEPT2/6/7 to the GDP-bound MT lattice may cause long-range conformational changes along MT protofilaments, affecting allosterically the binding of EB1 to plus ends. The latter would be consistent with a mechanical model of long-range coupling of conformational transitions between the tubulin subunits of MT protofilaments (Brouhard and Rice, 2018; Zanic et al., 2013), which is challenging to resolve experimentally.

To examine whether EB1-MT binding is inhibited through a direct interaction between SEPT2/6/7 and EB1, we performed protein-binding assays with EB1 and SEPT2/6/7 (5 µg each) in buffers of two different ionic conditions including those of the TIRF in vitro assay. In neither of these conditions, SEPT2/6/7 interacted with EB1 (Figure S3a). In contrast, we were able to detect an association between EB1 and SEPT5 (Figure S3b,c), a septin that possess the EB1-interaction motif SxIP (Honnappa et al., 2009; Jiang et al., 2012). To further test for a potential EB1-SEPT2/6/7 interaction, recombinant mCherry-SEPT2/6/7 was immobilized to functionalized glass substrata and binding of EB1-GFP was assessed microscopically in buffer conditions of the MT dynamics assay (data not shown). In this assay, binding was barely above background levels

bioRxiv preprint doi: https://doi.org/10.1101/638296; this version posted May 14, 2019. The copyright holder for this preprint (which was not certified by peer review) is the author/funder. All rights reserved. No reuse allowed without permission.

when high concentrations of SEPT2/6/7 (800 nM) were used in the presence of EB1 (75 nM). Taken together, these results suggest that SEPT2/6/7 is unlikely to inhibit EB1-MT binding through a direct interaction.

Next, we tested the possibility of a competition between EB1 and SEPT2/6/7 for binding to MTs using GMPCPP- and GTPγS-stabilized MTs, which respectively mimic the GTP-bound (low EB1 affinity) and GDP-Pi-bound (high EB1 affinity) conformations of polymerized tubulin (Maurer et al., 2011; Maurer et al., 2012; Roth et al., 2018; Zanic et al., 2009). Unlike EB1, SEPT2/6/7 showed no preference between GMPCPP- and GTPγS-stabilized MTs (Figure 4c), indicating that SEP2/6/7 interacts with GTPγS-bound MT lattices as optimally as observed with the GMPCPP-stabilized MT seeds (Figure 4c). In a competition experiment, EB1-GFP (75 nM) was incubated together with increasing concentrations of mCherry-SEPT2/6/7 in the presence of GTPγS-stabilized MTs. Strikingly, decoration of MTs with EB1-GFP was reduced and SEPT2/6/7 accumulated to MTs with concomitant displacement of EB1-GFP (Figure 4d). Notably, a 62.3% and 81% reduction in EB1-GFP (75 nM) binding was observed by 100 nM and 800 nM of mCherry-SEPT2/6/7, respectively (Figure 4e). These data indicate that binding of EB1 and SEPT2/6/7 to MTs is in part mutually exclusive and SEPT2/6/7 inhibits MT-EB1 binding.

Despite the competition between EB1 and SEPT2/6/7 for binding to the lattice of GTPγS-stabilized MTs, which mimic the GDP-Pi segments of MT plus end tips (high affinity state of EB1) (Maurer et al., 2011), we were not able to observe any exchange between mCherry-SEPT2/6/7 and EB1-GFP on the tips of dynamic MTs. This might be due to the higher affinity of EB1 for GDP-Pi than SEPT2/6/7; note that full decoration of GTPγS MTs by EB1 is achieved in much lower concentrations than SEPT2/6/7 (Figure 4d). Even at high concentration of SEPT2/6/7, which were very effective in displacing EB1 from GTPγS-stabilized MTs, SEPT2/6/7 did not displace EB1 by replacing EB1 at MT plus ends. Taken together with lack of SEPT2/6/7 tracking on MT plus ends, our data suggest that SEPT2/6/7 may allosterically affect EB1 binding by causing long-range conformational changes on MT protofilaments.

bioRxiv preprint doi: https://doi.org/10.1101/638296; this version posted May 14, 2019. The copyright holder for this preprint (which was not certified by peer review) is the author/funder. All rights reserved. No reuse allowed without permission.

End-on collisions of MT plus ends with SEPT2/6/7 filaments results in pausing and EB1 dissociation

Although SEPT2/6/7 does not track with growing MT plus ends in cells or in vitro, MT plus ends have been observed to collide end-on with septins (Bowen et al., 2011; Nolke et al., 2016). We, therefore, sought to determine whether septin filaments can directly impact MT plus end dynamics during end-on encounters, which do not involve association of septin complexes with the MT lattice.

We reconstituted MT dynamics in the presence of septin filaments by immobilizing mCherry-SEPT2/6/7 and MT seeds on glass substrata. Upon introduction of soluble tubulin, we were able to visualize the polymerizing plus ends of MTs intersecting with filamentous septins. During these encounters, MT plus ends paused, continued to grow or depolymerized (Figure 5a). Quantification showed that 48% of encounters resulted in MT plus pausing, while continuation of growth and depolymerization were observed at 37% and 14% of intersections, respectively. Strikingly, MT pausing events were significantly higher (2-fold) compared to plus end collisions with immobilized actin filaments (Fig. 5b). Upon encountering F-actin, continuation of MT plus end growth was much more frequent than pausing – pausing events (23%) were vastly significantly outnumbered by continued growth (74%), which was 3-fold more frequent (Figure 5b). In contrast, pausing events (48%) prevailed over continued growth (37%) at intersections with SEPT2/6/7 filaments (Figure 5a,b).

Next, we asked whether MT plus ends exhibited similar behavior upon encountering septin and actin filaments in the presence of EB1-GFP. Interestingly, EB1-bound MT plus ends paused less at both septin and F-actin intersections; EB1 also decreased the depolymerization events observed at septin filaments (Figure 5c-d). However, EB1-bound plus ends still paused more at collisions with septin than actin filaments (27.1% vs. 12.37%). Moreover, dissociation of EB1 from plus ends was more frequent at collisions with SEPT2/6/7 than actin filaments. In agreement with these in vitro observations, imaging of EB3-tdTomato comets was very frequent (79% of time)

bioRxiv preprint doi: https://doi.org/10.1101/638296; this version posted May 14, 2019. The copyright holder for this preprint (which was not certified by peer review) is the author/funder. All rights reserved. No reuse allowed without permission.

during collisions with GFP-SEPT7 in the neurites of hippocampal neurons. Kymographs showed EB3 comets pausing and ultimately disappearing upon contact with SEPT7, resembling in behavior the pausing and EB1 dissociation observed in our in vitro assays. These data demonstrate that septins can trigger plus end pausing and EB1 dissociation through *cis* and *trans* interaction with the MT lattice and plus end, respectively.

Discussion

A growing number of studies implicate septins in MT organization and dynamics as well as MT-dependent functions, but how septins impact the dynamic instability of MTs is not well understood. Results from cell biological experiments have been difficult to interpret as septins are multifunctional proteins with various binding partners, several of which associate with the cytoskeleton. Hence, in vitro reconstitution experiments can provide valuable insights by elucidating the direct effects of septins on MT dynamics.

In this study, MT dynamics were reconstituted with SEPT2/6/7 complexes and filaments. Our results suggest that the effects of SEPT2/6/7 on MT dynamics is dependent on their concentration and state of assembly. We found a biphasic graded effect on MT dynamics which correlated with a concentration-dependent assembly of SEPT2/6/7 into higher-order filaments. At lower concentrations (10-100 nM), where assembly of SEPT2/6/7 complexes into higher-order filaments is limited, MT growth and elongation were enhanced. However, at higher concentrations (low μM), which enhance the filamentous state of SEPT2/6/7, MT growth was stunted. Interestingly, in the intermediate range of concentrations, SEPT2/6/7 functions as a pausing factor, causing transient arrests of MT plus end growth. These effects of SEPT2/6/7 have both striking similarities and differences with SEPT9. While both SEPT2/6/7 heteromers and SEPT9 homomers promote the growing phase of MTs, SEPT2/6/7 achieves this effect at significantly lower concentrations than SEPT9. Moreover, micromolar concentrations of SEPT9 stabilize elongated MTs, which seize to grow and shrink, while micromolar SEPT2/6/7 dampens MT

bioRxiv preprint doi: https://doi.org/10.1101/638296; this version posted May 14, 2019. The copyright holder for this preprint (which was not certified by peer review) is the author/funder. All rights reserved. No reuse allowed without permission.

dynamics without stabilizing MTs that undergo more catastrophe. In addition to these differences, SEPT9 binds and recruits unpolymerized tubulin to the lattice of MTs, while SEPT2/6/7 does not bind unpolymerized tubulin. Conversely, submicromolar concentrations of SEPT2/6/7 can pause MT plus end growth, which was not observed with SEPT9. Taken together, these data indicate that there are septin subunit and paralog specific differences in the modulation of MT dynamics, which might be physiologically relevant for the modulation of MT dynamics in cell types and pathological conditions with distinct patterns of septin expression.

Our results show that SEPT2/6/7 can trigger dissociation of EB1 from MT plus ends in *cis* by binding to the lattice of plus ends or *in trans* by coming in contact as a filamentous structure with on-coming MT plus ends. A similar effect has been shown for tau, which antagonizes EB1-binding to plus ends (Ramirez-Rios et al., 2016). However, unlike tau which inhibits EB1-MT binding by forming a soluble complex with EB1 off MTs, SEPT2/6/7 does not appear to sequester EB1 off MTs. Interestingly, SEPT2/6/7 competes with EB1 for binding to GTPγS-stabilized MTs, which resemble the EB1-prefered tubulin-GDP-Pi conformation of plus end tips. Despite this finding, SEPT2/6/7 tracking on MT plus ends is rare and we found no evidence of direct competition between SEPT2/6/7 and EB1 at MT plus ends. Hence, we posit that the binding of SEPT2/6/7 to the MT-GDP lattice may result in conformational changes, which are propagated allosterically along protofilaments to plus ends (Brouhard and Rice, 2018). Evidence for this mechanism comes from studies of the potent MT polymerase XMAP215 and EB1 (Zanic et al., 2013). Even though XMAP215 and EB1 do not interact, a synergistic effect is posited to occur through conformational changes. Functionally, a septin-mediated dissociation of EB1 from MT plus ends could provide a mechanism for pausing and stable capture of MT plus ends. Given that EB1 appears to protect MT plus ends from pausing during end-on collisions with septin and actin filaments (see Figure 5), EB1 dissociation through *cis* or *trans* septin interactions with MTs would further enhance pausing of MT plus ends upon contact with septin filaments.

bioRxiv preprint doi: https://doi.org/10.1101/638296; this version posted May 14, 2019. The copyright holder for this preprint (which was not certified by peer review) is the author/funder. All rights reserved. No reuse allowed without permission.

How are the concentration-dependent effects that septins exert on MT plus ends in vitro relevant to the concentration, organization and localization of septins in living cells? MT growth and elongation are enhanced at septin concentrations of hundreds of nanomolar, which reportedly is the estimated concentration of septins such as SEPT2 (793 nM), SEPT6 (216 nM), SEPT7 (516 nM) and SEPT9 (417 nM) in HeLa cells (Hein et al., 2015). By contrast, micromolar septin concentrations dampen MT dynamics, resulting in stunted growth or complete MT stabilization. Given that septins are not uniformly distributed in cells and are enriched in specific subcellular regions (e.g., membrane domains of micron-scale curvature), it is plausible that septins tune MT dynamics in a region-specific manner according to their local concentration. Therefore, persistent MT growth could occur in cytoplasmic areas of moderate septin concentration, while MT pausing and stabilization could occur at cytoplasmic and membrane regions of septin enrichment. The latter could be key for the capture of MT plus ends at the base of membrane protrusions, where septins accumulate at domains of micron-scale curvature (Akil et al., 2016; Bridges et al., 2016; Cannon et al., 2019; Dolat and Spiliotis, 2016; Steels et al., 2007; Zhang et al., 1999), or the stabilization and dampening of MT plus end dynamics at the tips of primary cilia, in which septins are also highly enriched (Fliegauf et al., 2014; Ghossoub et al., 2013; Hu et al., 2010).

Additionally, the state of septin assembly may further impact the effects on MT dynamics as our data show that SEPT2/6/7 complexes assemble into short filaments at concentrations and conditions that promote MT growth. While high resolution EM is required to determine the organization of septins on the lattice of MTs, the assembly status of septins on and off MTs could play a role in the modulation of MT dynamics in health and disease. As septins have been identified in the neurofibrillary tangles and Lewy bodies of Alzheimer's and Parkinson's patient brains (Ihara et al., 2003; Ihara et al., 2007; Kinoshita et al., 1998; Shehadeh et al., 2009), filamentous aggregates of septins could have adverse effects on MT dynamics exacerbating the cytotoxicity and pathological progression of neurodegenerative disorders.

bioRxiv preprint doi: https://doi.org/10.1101/638296; this version posted May 14, 2019. The copyright holder for this preprint (which was not certified by peer review) is the author/funder. All rights reserved. No reuse allowed without permission.

MATERIALS AND METHODS

Plasmids

Plasmids encoding for recombinant His-tagged mouse SEPT2_i1 and SEPT6/7-strep tagged were a gift from Dr. Amy Gladfelter (University of North Carolina, Department of Biology) and were cloned into the pnEA-vH and pnCs vectors, respectively. Plasmid encoding for the recombinant His-tagged mouse SEPT2_i1-mCherry was a gift from Dr. Shae Padrick (Drexel University, College of Medicine) and was cloned into the pet15b vector. Plasmid encoding for GST-tagged EB1 was a gift from Dr. Anna Akhmanova (Utrecht University, Department of Biology) and was cloned into the pGEX-3x vector. Plasmid encoding for recombinant His-tagged GFP-EB1 was a gift from Dr. Antonina Roll-Mecak (NIH, Cell Biology and Biophysics) and was cloned into the pET21a vector. EB3-tdTomato was purchased from Addgene (tdTomato-N1-EB3; #50708, deposited by the Erik Dent lab). Plasmid encoding rat EGFP-SEPT7 was a kind gift from Dr. Lily Y. Jan and Dr. Yuh-Nung Jan (UCSF, Department of Physiology) (Yadav et al., 2017). His-tagged SEPT5 plasmid was constructed by PCR amplifying SEPT5 from pCMV-Myc-tagged SEPT5 (Addgene; #27272, deposited by Harish Pant lab) using the primers 5'-ATG GGT CGC GGA TCC GAA ATG AGC ACA GGC CTG-3' and 5'-CTC GAG TGC GGC CGC ATC ACT GGT CCT GCA TC-3' and inserting the fragment into the pET28a(+) vector. SEPT6/SEPT7 full length-strep tagged was constructed using a four-step KAPA Biosystems Site-directed mutagenesis protocol. Briefly, SEPT6/7-strep tagged was amplified with KAPA HiFi HotStart DNA polymerase (KK2502; KAPA BIOSYSTEMS) using the primers 5'-GTAATAATTTTGTTTAACTTTAAGAAGGAGATATACATATGTCGGTCAGTATGGTAGCTCAA CAGAAGAA-3' and 5'-TTCTTCTGTTGAGCTACCATACTGACCGACATATGTATATCTCCTTCTTAAAGTTAAACAAAA TTATTAC-3', to insert the first 12 bp (1-12 bp) at the N-terminus of SEPT7. The amplified PCR product was treated with DpnI (R0176L; New England Biolabs) for 1h at 37°C. DpnI-treated product was heat inactivated at 80°C for 20 min and subsequently was transformed in *E.coli* DH5a

bioRxiv preprint doi: https://doi.org/10.1101/638296; this version posted May 14, 2019. The copyright holder for this preprint (which was not certified by peer review) is the author/funder. All rights reserved. No reuse allowed without permission.

cells. The new construct was used as a template and amplified using the primers 5'-GATATACATATGTCGGTCAGTGCGAGATCCGCTGCTATGGTAGCTCAACAGAAGAAC-3' and 5'-GTTCTTCTGTTGAGCTACCATAGCAGCGGATCTCGCACTGACCGACATATGTATATC-3', in order to insert the next 15 bp (13-27 bp) of SEPT7. Subsequently, the pcr product was treated as above and used as a template to introduce the next 18 bp (28-45 bp) of SEPT7 using the primers 5'-TGCGAGATCCGCTGCTGCTGAGGAGAGGAGCGTCATGGTAGCTCAACAGA-3' and 5'-TCTGTTGAGCTACCATGACGCTCCTCTCCTCAGCAGCAGCGGATCTCGCA-3'. Finally, the resulted construct was used as a template and amplified using the primers 5'-TGAGGAGAGGAGCGTCAACAGCAGCACCATGGTAGCTCAACAGA-3' and 5'-TCTGTTGAGCTACCATGGTGCTGCTGTTGACGCTCCTCTCCTCA-3', to insert the last 12 bp (46-57 bp) of SEPT7.

Protein expression and purification

Recombinant His-tagged SEPT2/6/7-strep tagged (SEPT7 full length) complex was prepared as described before (Mavrakis et al., 2014). His-tagged SEPT2 or His-tagged SEPT2-mCherry and SEPT6/7-strep tagged were co-transformed into *E.coli* Bl21 (DE3) (Invitrogen). Bacterial cultures were grown to OD_{600} of 2-3 and induced with 1 mM IPTG for 1h at 37°C or OD_{600} of 0.5 and induced with 0.2 mM IPTG for 16 h at 18°C for fluorescently tagged His-tagged SEPT2-mCherry-SEPT6/7-strep. Cultures were centrifuged at 4,000 rpm for 20 min at 4°C. Pellets were resuspended in lysis buffer containing 50 mM Tris-HCl pH 8.0, 500 mM KCl, 10 mM imidazole, 5 mM $MgCl_2$, 1 mg/ml lysozyme, 1 mM PMSF and 1x Bacterial Protease Arrest protease inhibitor cocktail (G-Biosciences; 786-330) and lysed by sonication (10 sets of 15 pulses on ice with 30 s interval between each set). Cell lysates were centrifuged at 13,000 rpm for 30 min at 4°C and passed through a 0.45 µm pore filter. Supernatants were loaded onto gravity flow columns with Ni-NTA agarose beads (745400.25; Macherey-Nagel), which were equilibrated with 10 ml of

bioRxiv preprint doi: https://doi.org/10.1101/638296; this version posted May 14, 2019. The copyright holder for this preprint (which was not certified by peer review) is the author/funder. All rights reserved. No reuse allowed without permission.

buffer containing 50 mM Tris-HCl pH 8.0, 500 mM KCl, 10 mM imidazole, 5 mM $MgCl_2$, 1 mM PMSF and 1x Bacterial Protease Arrest protease inhibitor cocktail. Protein complexes were eluted in elution buffer containing 50 mM Tris-HCl pH 8.0, 500 mM KCl, 250 mM imidazole and 5 mM $MgCl_2$ and loaded to a StrepTrap HP column (GE Healthcare) equilibrated with buffer containing 50 mM Tris-HCl pH 8, 300 mM KCl and 5 mM $MgCl_2$. Protein complexes were eluted in elution buffer containing 50 mM Tris-HCl pH 8.0, 300 mM KCl, 5 mM $MgCl_2$ and 2.5 mM d-Desthiobiotin (SIGMA; D1411) and dialyzed overnight at 4ºC in BRB80 (80 mM Pipes pH 6.9, 2 mM $MgCl_2$, 1 mM EGTA). His-tagged SEPT2-mCherry-SEPT6/7-strep was further purified using an AKTA FPLC system (GE Healthcare) with a Superdex 200 10/300 GL (Amersham Biosciences) gel filtration column.

Recombinant His-tagged GFP-EB1 and His-tagged SEPT5 were transformed into *E.coli* Bl21 (DE3) (Invitrogen). Bacterial cultures were grown to OD_{600} of 0.6-0.8 and induced with 0.2 mM IPTG for 16 h at 18ºC for His-tagged GFP-EB1 or cultures were grown to OD_{600} of 0.4-0.6 and induced with 1 mM IPTG for 5 h at 23ºC for His-tagged SEPT5. Cultures were centrifuged at 4,000 rpm for 20 min at 4ºC. Pellets were resuspended in lysis buffer containing 50 mM Tris pH 8.0, 150 mM NaCl, 10% glycerol, 1 mM PMSF, 1 mg/ml lysozyme, 10 mM imidazole and 1x Bacterial Protease Arrest protease inhibitor cocktail (G-Biosciences; 786-330) and lysed by sonication (10 sets of 15 pulses on ice with 30 s interval between each set). Cell lysates were centrifuged at 13,000 rpm for 30 min at 4ºC and passed through a 0.45 µm pore filter. Supernatants were loaded onto gravity flow column with Ni-NTA agarose beads (745400.25; Macherey-Nagel), which were equilibrated with 10 ml of buffer containing 50 mM Tris pH 8.0, 150 mM NaCl, 10% glycerol, 1 mM PMSF, 10 mM imidazole and 1x Bacterial Protease Arrest protease inhibitor cocktail. Columns were washed with 30 ml washing buffer (50 mM Tris pH 8.0, 300 mM NaCl, 10% glycerol, 10 mM imidazole). Proteins were eluted in elution buffer containing 50 mM Tris pH 8.0, 150 mM NaCl, 10% glycerol and 250 mM imidazole. His-tagged GFP-EB1 was dialyzed overnight at 4ºC in BRB80 (80 mM Pipes pH 6.9, 2 mM $MgCl_2$, 1 mM EGTA) supplemented with 50 mM KCl

bioRxiv preprint doi: https://doi.org/10.1101/638296; this version posted May 14, 2019. The copyright holder for this preprint (which was not certified by peer review) is the author/funder. All rights reserved. No reuse allowed without permission.

and was further purified using an AKTA FPLC system (GE Healthcare) with a Superdex 200 10/300 GL (Amersham Biosciences) gel filtration column. His-tagged SEPT5 was dialyzed overnight at 4ºC in buffer containing 50 mM Tris pH 8.0, 150 mM NaCl, 10% glycerol.

Recombinant GST and GST-tagged EB1 were transformed into *E.coli* Bl21 (DE3) (Invitrogen). Bacterial cultures were grown to OD_{600} of 0.7 and induced with 1 mM IPTG for 5.5 h at 25ºC. Cultures were centrifuged at 4,000 rpm for 20 min at 4ºC. Cell pellets were resuspended in lysis buffer containing 50 mM Tris pH 8.0, 150 mM NaCl, 2 mM $MgCl_2$, 5 mM DTT, 10% glycerol, 0.1% Triton X-100, 1 mM PMSF, 1 mg/ml lysozyme and 1x Bacterial Protease Arrest protease inhibitor cocktail (G-Biosciences; 786-330) and lysed by sonication (10 sets of 15 pulses on ice with 30 s interval between each set). Cell lysates were centrifuged at 13,000 rpm for 30 min at 4oC and passed through a 0.45 µm pore filter. Supernatants were loaded onto gravity flow columns with Glutathione agarose beads (16100; Thermo Scientific) equilibrated with 10 ml of buffer containing 50 mM Tris pH 8.0, 150 mM NaCl, 2 mM $MgCl_2$, 5 mM DTT, 10% glycerol, 0.1% Triton X-100, 1 mM PMSF and 1x Bacterial Protease Arrest protease inhibitor cocktail. Subsequently, columns were washed with 30 ml washing buffer (50 mM Tris pH 8.0, 150 mM NaCl, 2 mM $MgCl_2$, 5 mM DTT, 10% glycerol and 0.1% Triton X-100) and proteins were eluted in elution buffer containing 50 mM Tris pH 8.0, 150 mM NaCl, 2 mM $MgCl_2$, 5 mM DTT, 10% glycerol and 10 mM glutathione. All proteins were dialyzed overnight at 4ºC in buffer containing 50 mM Tris pH 8.0, 150 mM NaCl and 10% glycerol.

Recombinant His-tagged SEPT9_i1 was expressed and purified as described before (Nakos et al., 2019).

GST-pull down assays

Protein-protein interaction assays were performed between GST or GST-tagged EB1 and His-tagged SEPT2/6/7-strep or His-tagged SEPT5 proteins. 5µg of GST or GST-EB1 were incubated with 20 µl glutathione agarose beads (16100; Thermo Scientific) for 2 h at 4ºC. Subsequently,

bioRxiv preprint doi: https://doi.org/10.1101/638296; this version posted May 14, 2019. The copyright holder for this preprint (which was not certified by peer review) is the author/funder. All rights reserved. No reuse allowed without permission.

beads were washed twice with pull down buffer (50 mM Hepes pH 7.4, 150 mM NaCl, 0.1% Triton X-100, 1 mM PMSF, 5 mM DTT, 2 mM EGTA and 10% glycerol) or BRB80 supplemented with 0.1% Triton X-100, 1 mM PMSF and 50 mM KCl. Beads were incubated with 5 µg His-SEPT2/6/7-strep or His-SEPT5 for 2 h at 4ºC. Beads were washed five times with pull down buffer or BRB80 (with 0.1% Triton X-100, 1 mM PMSF and 50 mM KCl) before they were resuspended with loading buffer and boiled. Eluted complexes loaded onto 10% SDS-PAGE gels and transferred to a nitrocellulose membrane. Membranes were blocked with 5% non-fat dry milk and 1% BSA for 1 h at room temperature. Membranes were washed with PBS-T (PBS1x/0.1% Tween 20) and incubated with mouse antibody against 6xHis-tag (1:2,000; Qiagen), rabbit antibody against GST-tag (1:10,000; Santa Cruz) or rabbit antibody against SEPT7 (1:10,000; IBL) diluted in PBS-T/2% BSA over night at 4ºC. Subsequently, membranes were washed with PBS-T and incubated with anti-mouse or anti–rabbit secondary antibodies (LiCor) for 1 hour at room temperature, before scanning with an imaging system (Odyssey; LICOR).

Pelleting assay of recombinant SEPT2/6/7

In pelleting assays of recombinant His-SEPT2/6/7-strep, increasing concentrations of SEPT2/6/7 (10 nM – 4 µM) were incubated in BRB80 (80 mM Pipes pH 6.9, 2 mM $MgCl_2$, 1 mM EGTA) supplemented with 1 mM GTP for 15 min at room temperature. Reactions were placed on top of a cushion buffer and centrifuged at 15,600 x *g* (Optima TL100; Beckman Coulter) for 10 min at 25ºC. Equal volumes of supernatant and pellet fractions were loaded onto 8% SDS-PAGE gels which were stained with Coomassie Brilliant Blue. SDS-PAGE gels were scanned and protein bands were quantified with the Odyssey scanning system (LICOR).

TIRF assays of dynamic MTs

Imaging chambers were prepared and constructed as before (Nakos et al., 2019; Reid et al., 2016; Tanenbaum et al., 2013). TIRF imaging was performed as described before (Nakos et al.,

bioRxiv preprint doi: https://doi.org/10.1101/638296; this version posted May 14, 2019. The copyright holder for this preprint (which was not certified by peer review) is the author/funder. All rights reserved. No reuse allowed without permission.

2019). Imaging chambers were prepared by sequential treatment with the following buffers: 1% Pluronic F-127 for 5 min, 5 mg/ml Biotin-BSA (A8549; Sigma-Aldrich) for 5 min, and 0.5 mg/ml Neutravidin (A2666; Invitrogen) for 5 min. GMPCPP-stabilized microtubule seeds (~60-80 nM) were floated into the chamber for 15 min and then washed with blocking buffer (BRB80, 1% Pluronic F-127, 1 mg/ml BSA) for 5 min. GMPCPP MT seeds were prepared by incubating 77% unlabeled tubulin (T240, Cytoskeleton Inc.) with 11.5% biotin-tubulin (T333P, Cytoskeleton Inc.) and 11.5% HiLyte-488-tubulin (TL488M, Cytoskeleton Inc.) or 11.5% HiLyte-647-tubulin (TL670M, Cytoskeleton Inc.). The tubulin mix (20 μM) with 1 mM GMPCPP (NU-405L; Jena Bioscience) in BRB80 (80 mM Pipes pH 6.9, 2 mM $MgCl_2$, 1 mM EGTA) was incubated at 37°C for 30 min. After incubation, seeds were diluted in BRB80 and spun for 15 min at 100,000 g (Optima TL100; Beckman Coulter). Sedimented microtubule seeds were resuspended in 60μl of BRB80. In chambers, microtubule polymerization was induced by floating a mix of 10 μM tubulin, which contained 6.6% Rhodamine-tubulin (TL590M; Cytoskeleton Inc.) or HiLyte-488-tubulin (TL488M; Cytoskeleton Inc.) in BRB80 with 1 mM GTP, 0.1 mg/ml BSA, 0.1% Pluronic F-127, 0.1% κ-casein, 0.2% methyl cellulose, oxygen scavenging system (0.5 mg/ml glucose oxidase, 0.1 mg/ml catalase, 4.5 mg/ml D-glucose, 70 mM β-mercaptoethanol) and recombinant His-SEPT2/6/7-strep or His-SEPT2-mCherry-6/7-strep proteins.

For TIRF assays with His-GFP-EB1 and His-SEPT2-mCherry-6/7-strep proteins, GMPCPP MT bright seeds were prepared as described above by incubating 66.7% unlabeled tubulin (T240, Cytoskeleton Inc.) with 11.5% biotin-tubulin (T333P, Cytoskeleton Inc.) and 21.8% HiLyte-647-tubulin (TL670M, Cytoskeleton Inc.). Microtubule polymerization was induced by introducing a mix of 10 μM tubulin, which contained 4.67% HiLyte-647-tubulin (TL670M, Cytoskeleton Inc.) in BRB80 supplemented with 1 mM GTP, 0.1 mg/ml BSA, 0.1% Pluronic F-127, 0.1% κ-casein, 0.2% methyl cellulose, oxygen scavenging system (0.5 mg/ml glucose oxidase, 0.1 mg/ml catalase, 4.5 mg/ml D-glucose, 70 mM β-mercaptoethanol), 50 mM KCl and recombinant His-SEPT2-mCherry-

bioRxiv preprint doi: https://doi.org/10.1101/638296; this version posted May 14, 2019. The copyright holder for this preprint (which was not certified by peer review) is the author/funder. All rights reserved. No reuse allowed without permission.

6/7-strep and His-GFP-EB1 proteins. Imaging chambers were sealed with vacuum grease prior to imaging at 37ºC. Imaging was performed every 2 s for 15 min.

TIRF septin-tubulin binding assays

Imaging of unpololymerized soluble tubulin binding to septins by TIRF imaging was performed by adapting a previous MT nucleation assay (Lazarus et al., 2013). Imaging chambers were constructed using acid washed slides and silanized glass cover slips. Acid washed glass coverslips were incubated for 10 min with 20% 3-Aminopropyltriethoxysilane (430941000; ACROS Organics) diluted in acetone and subsequently washed with ddH_2O for 15 min. Imaging chambers were first incubated with 1% Pluronic F-127 for 5 min. Chambers were washed with BRB80 and then were coated with mouse antibody against 6xHis-tag (1:50; Qiagen) for 10 min. Imaging chambers were washed with BRB80 and blocked with 5% Pluronic F-127 for 5 min. Flow chambers were washed with BRB80-1mg/ml BSA and subsequently incubated for 15 min with increasing concentrations of His-SEPT9 or His-SEPT2/6/7-strep. Unbound proteins were removed from chambers with multiple washes of BRB80-1mg/ml BSA. Reactions were initiated with the introduction of a tubulin mix (3.5 μM), which contained 8.6% Rhodamine-tubulin (TL590M; Cytoskeleton Inc.) in BRB80 supplemented with 2.5 mM GTP, 1 mg/ml BSA, 0.25% Pluronic F-127, 0.1% κ-casein and oxygen scavenging system (0.5 mg/ml glucose oxidase, 0.1 mg/ml catalase, 4.5 mg/ml D-glucose, 70 mM β-mercaptoethanol). Chambers were sealed with vacuum grease and imaging was performed at 37ºC, every 2 s for 15 min.

TIRF assays of dynamic MTs with S2/6/7 or F-actin filaments

GMPCPP MT seeds-HiLyte-647 labeled were made as described above. Imaging chambers were incubated first with 1% Pluronic F-127 for 5 min. Chambers were washed with BRB80 and then were coated with rabbit antibody against SEPT7 (1:10; IBL) for 10 min. Imaging chambers were washed with BRB80 and blocked with 5% Pluronic F-127 for 5 min. Flow chambers were washed

bioRxiv preprint doi: https://doi.org/10.1101/638296; this version posted May 14, 2019. The copyright holder for this preprint (which was not certified by peer review) is the author/funder. All rights reserved. No reuse allowed without permission.

with BRB80-1mg/ml BSA and subsequently incubated for 15 min with 800 nM of His-SEPT2-mCherry-6/7-strep. Unbound proteins were removed from chambers with multiple washes of BRB80-1mg/ml BSA. Imaging chambers were then incubated with 5 mg/ml Biotin-BSA (A8549; Sigma-Aldrich) for 5 min. Chambers were washed with BRB80-1mg/ml BSA and incubated with 0.5 mg/ml Neutravidin (A2666; Invitrogen) for 5 min. After wash with BRB80-1mg/ml BSA, chambers were incubated with blocking buffer (BRB80, 1% Pluronic F-127, 1 mg/ml BSA) for 5 min. Imaging chambers were washed again with BRB80-1mg/ml BSA and incubated with GMPCPP MT seeds-HiLyte-647-labeled diluted in BRB80-1mg/ml BSA for 15 min. Finally, microtubule polymerization was initiated by introducing a mix of 14 μM tubulin, which contained 9% HiLyte-488-tubulin (TL488M; Cytoskeleton Inc.) in BRB80 supplemented with 1 mM GTP, 1 mg/ml BSA, 0.25% Pluronic F-127, 0.1% κ-casein, 0.2% methyl cellulose and oxygen scavenging system (0.5 mg/ml glucose oxidase, 0.1 mg/ml catalase, 4.5 mg/ml D-glucose, 70 mM β-mercaptoethanol). For TIRF assays in the presence of His-GFP-EB1, bright GMPCPP MT seeds-HiLyte-647-labeled and dim dynamic MTs-Hilyte-647-labeled were used. Microtubule polymerization reaction was additionally supplemented with 75 nM His-GFP-EB1 and 50 mM KCl. Chambers were sealed with vacuum grease and imaging was performed at 37°C, every 2 s for 15 min.

TIRF assays that performed in the presence of F-actin served as control. F-actin filaments (28 μM) were made by incubating 83% unlabeled G-actin (APHL99; Cytoskeleton Inc.) with 8.5% biotin-G-actin (AB07; Cytoskeleton Inc.) and 8.5% Rhodamine-G-actin (APHR; Cytoskeleton Inc.) in the presence of F-actin buffer (20 mM Hepes pH 7.4, 100 mM KCl, 1 mM $MgCl_2$, 0.5 mM ATP and 4 mM DTT) for 1 h at room temperature. Imaging chambers were treated as above but with the following differences; 1) chambers were not coated with an antibody and 2) 50 nM of Rhodamine F-actin filaments were mixed with GMPCPP MT seeds-HiLyte-647-labeled and incubated for 25 min. Microtubule polymerization reaction was initiated as described above.

bioRxiv preprint doi: https://doi.org/10.1101/638296; this version posted May 14, 2019. The copyright holder for this preprint (which was not certified by peer review) is the author/funder. All rights reserved. No reuse allowed without permission.

In vitro TIRF SEPT2/6/7 filaments-EB1 interaction.

As described above imaging chambers were incubated sequentially with: 1% Pluronic F-127 for 5 min. Chambers were washed with BRB80 and then were coated with rabbit antibody against SEPT7 (1:10; IBL) for 10 min. Imaging chambers were washed with BRB80 and blocked with 5% Pluronic F-127 for 5 min. Flow chambers were washed with BRB80-1mg/ml BSA and subsequently incubated for 15 min with increased concentrations of His-SEPT2-mCherry-6/7-strep. Unbound proteins were removed from chambers with multiple washes of BRB80-1mg/ml BSA. Reactions were initiated with the introduction of a mix contained BRB80 supplemented with 1 mg/ml BSA, 0.25% Pluronic F-127, 0.1% κ-casein and oxygen scavenging system (0.5 mg/ml glucose oxidase, 0.1 mg/ml catalase, 4.5 mg/ml D-glucose, 70 mM β-mercaptoethanol) supplemented with 75 nM His-GFP-EB1 and 50 mM KCl. Chambers were sealed with vacuum grease and imaging was performed at 25ºC, every 2 s for 15 min.

Mixed-lattice TIRF-binding assays

For mixed-lattice binding assays, GMPCPP and GTPγS seeds were prepared similar to (Roth et al., 2018). GMPCPP and GTPγS MT seeds were made by incubating 77% unlabeled tubulin (T240, Cytoskeleton Inc.) with 11.5% biotin-tubulin (T333P, Cytoskeleton Inc.) and 11.5% HiLyte-647-tubulin (TL670M, Cytoskeleton Inc.) or 11.5% HiLyte-488-tubulin (TL488M, Cytoskeleton Inc.) on ice for 30 min in the presence of 1 mM GMPCPP or GTPγS (371545; EMD Millipore). Subsequently, tubulin mixes were placed at 37ºC for 30 min. Then 2 μM of taxol was added to each mix and seeds were further incubated for an additional 5 min at 37ºC. MT seeds were diluted in BRB80-2 μM taxol and centrifuged at 100,000 g (Optima TL100; Beckman Coulter) for 15 min. Pelleted microtubule seeds were resuspended in 60μl of BRB80-2 μM taxol. Imaging chambers were incubated sequentially with 1% Pluronic F-127 for 5 min, 5 mg/ml Biotin-BSA (A8549; Sigma-Aldrich) for 5 min, 0.5 mg/ml Neutravidin (A2666; Invitrogen) for 5 min, ~60 nM of both GMPCPP and GTPγS (mix 1:1) or ~60 nM of GTPγS MT seeds supplemented with 2 μM taxol for

bioRxiv preprint doi: https://doi.org/10.1101/638296; this version posted May 14, 2019. The copyright holder for this preprint (which was not certified by peer review) is the author/funder. All rights reserved. No reuse allowed without permission.

15 min and blocking buffer (BRB80, 1% Pluronic F-127, 1 mg/ml BSA, 2 μM taxol) for 5 min. To test His-SEPT2-mCherry-6/7-strep binding on GMPCPP and GTPγS MT seeds, increasing concentrations of His-SEPT2-mCherry-6/7-strep were incubated for 15 min with GMPCPP and GTPγS MT seeds in buffer containing BRB80, 0.1 mg/ml BSA, 0.1% Pluronic F-127, 0.1% κ-casein, oxygen scavenging system (0.5 mg/ml glucose oxidase, 0.1 mg/ml catalase, 4.5 mg/ml D-glucose, 70 mM β-mercaptoethanol) and 2 μM taxol. Imaging chambers were sealed with vacuum grease and still images were taken at 15 min of incubation.

For the competition assay, 75 nM of His-GFP-EB1 were incubated for 15 min with GTPγS MT seeds in the presence of increasing concentrations of His-SEPT2-mCherry-6/7-strep in a buffer containing BRB80, 0.1 mg/ml BSA, 0.1% Pluronic F-127, 0.1% κ-casein, 50 mM KCl, oxygen scavenging system (0.5 mg/ml glucose oxidase, 0.1 mg/ml catalase, 4.5 mg/ml D-glucose, 70 mM β-mercaptoethanol) and 2 μM taxol. Imaging chambers were sealed with vacuum grease and still images were taken at 15 min of incubation.

Primary Cultures and Transfection

Primary rat hippocampal cultures were obtained from the Neuron Culture Service Center (University of Pennsylvania). Hippocampi were dissected from embryonic day 18 pups of mixed genders, obtained from timed pregnant Sprague-Dawley rats. Cells were dissociated by incubation in trypsin-containing media. Cells were plated in Neurobasal medium supplemented with 2% B27 supplement (ThermoFisher). Cells were cultured in 24 well plates on 12 mm round glass coverslips (Bellco Glass, Inc.), coated with 1 mg/mL poly-L-Lysine (Peptides International). After 1 day in culture, cytosine d-D-arabinofuranoside (Sigma) was added at a final concentration of 1.5 μM to inhibit glial proliferation. Cells were maintained at 37ºC in a 5% CO_2 incubator. Neurons were cultured for 1-4 days in vitro (DIV) and transfected with Lipofectamine 3000 (Invitrogen) for 48 h (DIV3-6) before live imaging.

bioRxiv preprint doi: https://doi.org/10.1101/638296; this version posted May 14, 2019. The copyright holder for this preprint (which was not certified by peer review) is the author/funder. All rights reserved. No reuse allowed without permission.

Imaging of rat hippocampal neurons

Live-cell imaging of hippocampal neurons was performed on DIV 3-6, 48 h after transfection. Coverslips were mounted on bottomless 35 mm dishes with a 7 mm microwell using silicone vaccum grease (Beckman Coulter). Conditioned media from the coverslip's well, along with 2 mL of phenol red-free Neurobasal media supplemented with 2% B27 (Invitrogen) and 30 mM HEPES (Sigma, 1M stock). Dishes were sealed with ParaFilm. Cells were selected for moderate expression of both GFP-SEPT7 and EB3-tdTomato. Neurons were imaged at 30 frames per minute for 3 minutes using total internal reflection fluorescence (TIRF) imaging at 37ºC using the TIRF module on the DeltaVision OMX V4 inverted microscope equipped with an Olympus 60x/1.49 objective and a temperature controlled stage-top incubator.

All TIRF microscopy assays were performed with the DeltaVision OMX V4 inverted microscope (GE Healthcare) equipped with 60x/1.49 NA TIRF objective lens (Olympus), motorized stage, sCMOS pco.edge cameras (PCO), stage top incubator with temperature controller and the softWoRx software.

Image and statistical analyses

Quantifications of MT dynamics and fluorescence intensities were performed in ImageJ/Fiji. Time-lapse image series were corrected for bleaching using the bleach correction plugin. Kymograph analysis was used to quantify MT dynamics were with the KymographBuilder plugin. Growth and depolymerization rates were derive by manual segmentation of the trajectories of growing and shrinking MT plus ends, respectively. The Velocity measurement tool macro was used to calculate speed measurements. Pause events were excluded from growth and depolymerization rates. Catastrophe frequencies were measured by dividing the total number of catastrophe events by the total time spent in growing and pausing. Pauses were defined as events without change in the microtubule length for at least 40 s or more.

bioRxiv preprint doi: https://doi.org/10.1101/638296; this version posted May 14, 2019. The copyright holder for this preprint (which was not certified by peer review) is the author/funder. All rights reserved. No reuse allowed without permission.

Still images at 15 min of incubation were used to quantify the number of tubulin puncta bound to His-tagged SEPT2/6/7-strep or His-tagged SEPT9 (Figure S2). Background fluorescence was removed using the subtract background tool (rolling ball radius, 50 pixels) in Fiji. Manual fluorescence thresholding was applied and the analyze particles tool was used to count the number of tubulin puncta.

Quantification of the fluorescence intensity of His-tagged GFP-EB1 (Figure 4b) was performed similar to as described before (Ramirez-Rios et al., 2016). Background fluorescence was removed with the subtract background tool (rolling ball radius, 20 pixels) and fluorescence intensities of GFP-EB1 were measured from kymographs. Segmented lines of a 5-pixel width were drawn manually at the microtubule plus end tips and maximum fluorescence intensities were measured. Fluorescence intensities of His-tagged SEPT2-mCherry-6/7-strep were measured from still images at 15 min (Figure 3f and 4c). Segmented lines of equal width (5 pixels) were drawn manually along the entire length of GMPCPP MT seeds and the entire length of the lattice of plus end segments. The average pixel intensity was derived after subtraction of the average pixel intensity of background fluorescence, which was quantified by taking the mean value from three regions that did not contain any MTs. The same method was used to measure the average pixel intensity of His-tagged GFP-EB1 on GTPγS MT seeds (Figure 4e) in the presence of increasing concentrations of His-tagged SEPT2-mCherry-6/7-strep. Line scans (intensity vs distance plots) in Figure 3e were generated using the plot profile function in Fiji.

Analysis of EB3-tdTomato comet interaction with GFP-SEPT7 filaments in rat hippocampal neurons was done by making kymographs of neurites from time-lapse TIRF imaging movies using the Segmented Line (15 pixel width) and KymographBuilder tools in Fiji. Kymographs were treated as regions of interest (ROIs), and pause events were catalogued within these ROIs, describing

bioRxiv preprint doi: https://doi.org/10.1101/638296; this version posted May 14, 2019. The copyright holder for this preprint (which was not certified by peer review) is the author/funder. All rights reserved. No reuse allowed without permission.

which frame the pause began, when it ended, and whether the paused comet colocalized with GFP-SEPT7. A pause in these movies is defined as a halt in comet movement lasting longer than 3 frames (6 seconds).

Statistical analysis was performed using GraphPad Prism software. Each data set was tested for normal distribution using the Kolmogorov–Smirnov test. Mean, SEM, and *p* values were derived using Student's *t* test for normally distributed data and the Mann–Whitney *U* test for non-normally distributed data.

ACKNLOWLDGMENTS

We thank Dr. Shae Padrick (Drexel University, College of Medicine) for the plasmid encoding the His-tagged SEPT2-mCherry, Dr. Amy Gladfelter (University of North Carolina, Department of Biology) for the plasmid encoding SEPT6/7-strep, Dr. Antonina Roll-Mecak (NIH, Cell Biology and Biophysics) for the His-tagged GFP-EB1 plasmid, Dr. Anna Akhmanova (Utrecht University, Department of Biology) for the GST-tagged EB1 plasmid and Dr. Smita Yadav (University of Washington) for the plasmid encoding rat EGFP-SEPT7. All imaging was performed at Drexel University's Cell Imaging Center. This work was supported by NIH/NIGMS grant GM097664 to E.T.S. The authors have no conflict of interest to declare.

REFERENCES

1. Ageta-Ishihara, N., Miyata, T., Ohshima, C., Watanabe, M., Sato, Y., Hamamura, Y., Higashiyama, T., Mazitschek, R., Bito, H., and Kinoshita, M. (2013). Septins promote dendrite and axon development by negatively regulating microtubule stability via HDAC6-mediated deacetylation. Nat Commun *4*, 2532.

2. Akil, A., Peng, J., Omrane, M., Gondeau, C., Desterke, C., Marin, M., Tronchere, H., Taveneau, C., Sar, S., Briolotti, P.*, et al.* (2016). Septin 9 induces lipid droplets growth by a

bioRxiv preprint doi: https://doi.org/10.1101/638296; this version posted May 14, 2019. The copyright holder for this preprint (which was not certified by peer review) is the author/funder. All rights reserved. No reuse allowed without permission.

phosphatidylinositol-5-phosphate and microtubule-dependent mechanism hijacked by HCV. Nat Commun *7*, 12203.

3. Bai, X., Bowen, J.R., Knox, T.K., Zhou, K., Pendziwiat, M., Kuhlenbaumer, G., Sindelar, C.V., and Spiliotis, E.T. (2013). Novel septin 9 repeat motifs altered in neuralgic amyotrophy bind and bundle microtubules. J Cell Biol *203*, 895-905.

4. Bieling, P., Kandels-Lewis, S., Telley, I.A., van Dijk, J., Janke, C., and Surrey, T. (2008). CLIP-170 tracks growing microtubule ends by dynamically recognizing composite EB1/tubulin-binding sites. J Cell Biol *183*, 1223-1233.

5. Bieling, P., Laan, L., Schek, H., Munteanu, E.L., Sandblad, L., Dogterom, M., Brunner, D., and Surrey, T. (2007). Reconstitution of a microtubule plus-end tracking system in vitro. Nature *450*, 1100-1105.

6. Bowen, J.R., Hwang, D., Bai, X., Roy, D., and Spiliotis, E.T. (2011). Septin GTPases spatially guide microtubule organization and plus end dynamics in polarizing epithelia. J Cell Biol *194*, 187-197.

7. Bridges, A.A., Jentzsch, M.S., Oakes, P.W., Occhipinti, P., and Gladfelter, A.S. (2016). Micron-scale plasma membrane curvature is recognized by the septin cytoskeleton. J Cell Biol *213*, 23-32.

8. Brouhard, G.J., and Rice, L.M. (2018). Microtubule dynamics: an interplay of biochemistry and mechanics. Nat Rev Mol Cell Biol *19*, 451-463.

9. Cannon, K.S., Woods, B.L., Crutchley, J.M., and Gladfelter, A.S. (2019). An amphipathic helix enables septins to sense micrometer-scale membrane curvature. J Cell Biol *218*, 1128-1137.

10. Dixit, R., Barnett, B., Lazarus, J.E., Tokito, M., Goldman, Y.E., and Holzbaur, E.L. (2009). Microtubule plus-end tracking by CLIP-170 requires EB1. Proc Natl Acad Sci U S A *106*, 492-497.

11. Dolat, L., and Spiliotis, E.T. (2016). Septins promote macropinosome maturation and traffic to the lysosome by facilitating membrane fusion. J Cell Biol *214*, 517-527.

bioRxiv preprint doi: https://doi.org/10.1101/638296; this version posted May 14, 2019. The copyright holder for this preprint (which was not certified by peer review) is the author/funder. All rights reserved. No reuse allowed without permission.

12. Estey, M.P., Di Ciano-Oliveira, C., Froese, C.D., Bejide, M.T., and Trimble, W.S. (2010). Distinct roles of septins in cytokinesis: SEPT9 mediates midbody abscission. J Cell Biol *191*, 741-749.

13. Fliegauf, M., Kahle, A., Haffner, K., and Zieger, B. (2014). Distinct localization of septin proteins to ciliary sub-compartments in airway epithelial cells. Biol Chem *395*, 151-156.

14. Ghossoub, R., Hu, Q., Failler, M., Rouyez, M.C., Spitzbarth, B., Mostowy, S., Wolfrum, U., Saunier, S., Cossart, P., Jamesnelson, W.*, et al.* (2013). Septins 2, 7 and 9 and MAP4 colocalize along the axoneme in the primary cilium and control ciliary length. J Cell Sci *126*, 2583-2594.

15. Hein, M.Y., Hubner, N.C., Poser, I., Cox, J., Nagaraj, N., Toyoda, Y., Gak, I.A., Weisswange, I., Mansfeld, J., Buchholz, F.*, et al.* (2015). A human interactome in three quantitative dimensions organized by stoichiometries and abundances. Cell *163*, 712-723.

16. Honnappa, S., Gouveia, S.M., Weisbrich, A., Damberger, F.F., Bhavesh, N.S., Jawhari, H., Grigoriev, I., van Rijssel, F.J., Buey, R.M., Lawera, A.*, et al.* (2009). An EB1-binding motif acts as a microtubule tip localization signal. Cell *138*, 366-376.

17. Hu, Q., Milenkovic, L., Jin, H., Scott, M.P., Nachury, M.V., Spiliotis, E.T., and Nelson, W.J. (2010). A septin diffusion barrier at the base of the primary cilium maintains ciliary membrane protein distribution. Science *329*, 436-439.

18. Ihara, M., Tomimoto, H., Kitayama, H., Morioka, Y., Akiguchi, I., Shibasaki, H., Noda, M., and Kinoshita, M. (2003). Association of the cytoskeletal GTP-binding protein Sept4/H5 with cytoplasmic inclusions found in Parkinson's disease and other synucleinopathies. J Biol Chem *278*, 24095-24102.

19. Ihara, M., Yamasaki, N., Hagiwara, A., Tanigaki, A., Kitano, A., Hikawa, R., Tomimoto, H., Noda, M., Takanashi, M., Mori, H.*, et al.* (2007). Sept4, a component of presynaptic scaffold and Lewy bodies, is required for the suppression of alpha-synuclein neurotoxicity. Neuron *53*, 519-533.

bioRxiv preprint doi: https://doi.org/10.1101/638296; this version posted May 14, 2019. The copyright holder for this preprint (which was not certified by peer review) is the author/funder. All rights reserved. No reuse allowed without permission.

20. Janke, C., and Montagnac, G. (2017). Causes and Consequences of Microtubule Acetylation. Curr Biol *27*, R1287-R1292.

21. Jiang, K., Toedt, G., Montenegro Gouveia, S., Davey, N.E., Hua, S., van der Vaart, B., Grigoriev, I., Larsen, J., Pedersen, L.B., Bezstarosti, K.*, et al.* (2012). A Proteome-wide screen for mammalian SxIP motif-containing microtubule plus-end tracking proteins. Curr Biol *22*, 1800-1807.

22. Karasmanis, E.P., Phan, C., Angelis, D., Kesisova, I.A., Hoogenraad, C.C., McKenney, R.J., and Spiliotis, E.T. (2018). Polarity of neuronal membrane traffic requires sorting of kinesin motor cargo during entry into dendrites by a microtubule-associated protein. Developmental Cell, in press.

23. Kim, M.S., Froese, C.D., Estey, M.P., and Trimble, W.S. (2011). SEPT9 occupies the terminal positions in septin octamers and mediates polymerization-dependent functions in abscission. J Cell Biol *195*, 815-826.

24. Kinoshita, A., Kinoshita, M., Akiyama, H., Tomimoto, H., Akiguchi, I., Kumar, S., Noda, M., and Kimura, J. (1998). Identification of septins in neurofibrillary tangles in Alzheimer's disease. Am J Pathol *153*, 1551-1560.

25. Kinoshita, M. (2003a). Assembly of mammalian septins. J Biochem *134*, 491-496.

26. Kinoshita, M. (2003b). The septins. Genome Biol *4*, 236.

27. Kremer, B.E., Haystead, T., and Macara, I.G. (2005). Mammalian septins regulate microtubule stability through interaction with the microtubule-binding protein MAP4. Mol Biol Cell *16*, 4648-4659.

28. Lazarus, J.E., Moughamian, A.J., Tokito, M.K., and Holzbaur, E.L. (2013). Dynactin subunit p150(Glued) is a neuron-specific anti-catastrophe factor. PLoS Biol *11*, e1001611.

29. Maurer, S.P., Bieling, P., Cope, J., Hoenger, A., and Surrey, T. (2011). GTPgammaS microtubules mimic the growing microtubule end structure recognized by end-binding proteins (EBs). Proc Natl Acad Sci U S A *108*, 3988-3993.

bioRxiv preprint doi: https://doi.org/10.1101/638296; this version posted May 14, 2019. The copyright holder for this preprint (which was not certified by peer review) is the author/funder. All rights reserved. No reuse allowed without permission.

30. Maurer, S.P., Fourniol, F.J., Bohner, G., Moores, C.A., and Surrey, T. (2012). EBs recognize a nucleotide-dependent structural cap at growing microtubule ends. Cell *149*, 371-382.

31. Mavrakis, M., Azou-Gros, Y., Tsai, F.C., Alvarado, J., Bertin, A., Iv, F., Kress, A., Brasselet, S., Koenderink, G.H., and Lecuit, T. (2014). Septins promote F-actin ring formation by crosslinking actin filaments into curved bundles. Nat Cell Biol *16*, 322-334.

32. Menon, M.B., Sawada, A., Chaturvedi, A., Mishra, P., Schuster-Gossler, K., Galla, M., Schambach, A., Gossler, A., Forster, R., Heuser, M.*, et al.* (2014). Genetic deletion of SEPT7 reveals a cell type-specific role of septins in microtubule destabilization for the completion of cytokinesis. PLoS Genet *10*, e1004558.

33. Nakos, K., Rosenberg, M., and Spiliotis, E.T. (2019). Regulation of microtubule plus end dynamics by septin 9. Cytoskeleton (Hoboken) *76*, 83-91.

34. Nolke, T., Schwan, C., Lehmann, F., Ostevold, K., Pertz, O., and Aktories, K. (2016). Septins guide microtubule protrusions induced by actin-depolymerizing toxins like Clostridium difficile transferase (CDT). Proc Natl Acad Sci U S A *113*, 7870-7875.

35. Ostevold, K., Melendez, A.V., Lehmann, F., Schmidt, G., Aktories, K., and Schwan, C. (2017). Septin remodeling is essential for the formation of cell membrane protrusions (microtentacles) in detached tumor cells. Oncotarget *8*, 76686-76698.

36. Ramirez-Rios, S., Denarier, E., Prezel, E., Vinit, A., Stoppin-Mellet, V., Devred, F., Barbier, P., Peyrot, V., Sayas, C.L., Avila, J.*, et al.* (2016). Tau antagonizes end-binding protein tracking at microtubule ends through a phosphorylation-dependent mechanism. Mol Biol Cell *27*, 2924-2934.

37. Reid, T.A., Schuster, B.M., Mann, B.J., Balchand, S.K., Plooster, M., McClellan, M., Coombes, C.E., Wadsworth, P., and Gardner, M.K. (2016). Suppression of microtubule assembly kinetics by the mitotic protein TPX2. J Cell Sci *129*, 1319-1328.

bioRxiv preprint doi: https://doi.org/10.1101/638296; this version posted May 14, 2019. The copyright holder for this preprint (which was not certified by peer review) is the author/funder. All rights reserved. No reuse allowed without permission.

38. Roth, D., Fitton, B.P., Chmel, N.P., Wasiluk, N., and Straube, A. (2018). Spatial positioning of EB family proteins at microtubule tips involves distinct nucleotide-dependent binding properties. J Cell Sci *132*.

39. Russell, S.E., and Hall, P.A. (2011). Septin genomics: a road less travelled. Biol Chem *392*, 763-767.

40. Sellin, M.E., Sandblad, L., Stenmark, S., and Gullberg, M. (2011). Deciphering the rules governing assembly order of mammalian septin complexes. Mol Biol Cell *22*, 3152-3164.

41. Sellin, M.E., Stenmark, S., and Gullberg, M. (2012). Mammalian SEPT9 isoforms direct microtubule-dependent arrangements of septin core heteromers. Mol Biol Cell *23*, 4242-4255.

42. Sellin, M.E., Stenmark, S., and Gullberg, M. (2014). Cell type-specific expression of SEPT3-homology subgroup members controls the subunit number of heteromeric septin complexes. Mol Biol Cell *25*, 1594-1607.

43. Sheffield, P.J., Oliver, C.J., Kremer, B.E., Sheng, S., Shao, Z., and Macara, I.G. (2003). Borg/septin interactions and the assembly of mammalian septin heterodimers, trimers, and filaments. J Biol Chem *278*, 3483-3488.

44. Shehadeh, L., Mitsi, G., Adi, N., Bishopric, N., and Papapetropoulos, S. (2009). Expression of Lewy body protein septin 4 in postmortem brain of Parkinson's disease and control subjects. Mov Disord *24*, 204-210.

45. Silverman-Gavrila, R.V., and Silverman-Gavrila, L.B. (2008). Septins: new microtubule interacting partners. ScientificWorldJournal *8*, 611-620.

46. Sirajuddin, M., Farkasovsky, M., Hauer, F., Kuhlmann, D., Macara, I.G., Weyand, M., Stark, H., and Wittinghofer, A. (2007). Structural insight into filament formation by mammalian septins. Nature *449*, 311-315.

47. Spiliotis, E.T. (2018). Spatial effects - site-specific regulation of actin and microtubule organization by septin GTPases. J Cell Sci *131*.

bioRxiv preprint doi: https://doi.org/10.1101/638296; this version posted May 14, 2019. The copyright holder for this preprint (which was not certified by peer review) is the author/funder. All rights reserved. No reuse allowed without permission.

48. Spiliotis, E.T., Hunt, S.J., Hu, Q., Kinoshita, M., and Nelson, W.J. (2008). Epithelial polarity requires septin coupling of vesicle transport to polyglutamylated microtubules. J Cell Biol *180*, 295-303.

49. Spiliotis, E.T., Kinoshita, M., and Nelson, W.J. (2005). A mitotic septin scaffold required for Mammalian chromosome congression and segregation. Science *307*, 1781-1785.

50. Steels, J.D., Estey, M.P., Froese, C.D., Reynaud, D., Pace-Asciak, C., and Trimble, W.S. (2007). Sept12 is a component of the mammalian sperm tail annulus. Cell Motil Cytoskeleton *64*, 794-807.

51. Tanenbaum, M.E., Vale, R.D., and McKenney, R.J. (2013). Cytoplasmic dynein crosslinks and slides anti-parallel microtubules using its two motor domains. Elife *2*, e00943.

52. Targa, B., Klipfel, L., Cantaloube, I., Salameh, J., Benoit, B., Pous, C., and Baillet, A. (2019). Septin filament coalignment with microtubules depends on SEPT9_i1 and tubulin polyglutamylation, and is an early feature of acquired cell resistance to paclitaxel. Cell Death Dis *10*, 54.

53. Weirich, C.S., Erzberger, J.P., and Barral, Y. (2008). The septin family of GTPases: architecture and dynamics. Nat Rev Mol Cell Biol *9*, 478-489.

54. Yadav, S., Oses-Prieto, J.A., Peters, C.J., Zhou, J., Pleasure, S.J., Burlingame, A.L., Jan, L.Y., and Jan, Y.N. (2017). TAOK2 Kinase Mediates PSD95 Stability and Dendritic Spine Maturation through Septin7 Phosphorylation. Neuron *93*, 379-393.

55. Zanic, M., Stear, J.H., Hyman, A.A., and Howard, J. (2009). EB1 recognizes the nucleotide state of tubulin in the microtubule lattice. PLoS One *4*, e7585.

56. Zanic, M., Widlund, P.O., Hyman, A.A., and Howard, J. (2013). Synergy between XMAP215 and EB1 increases microtubule growth rates to physiological levels. Nat Cell Biol *15*, 688-693.

bioRxiv preprint doi: https://doi.org/10.1101/638296; this version posted May 14, 2019. The copyright holder for this preprint (which was not certified by peer review) is the author/funder. All rights reserved. No reuse allowed without permission.

57. Zhang, J., Kong, C., Xie, H., McPherson, P.S., Grinstein, S., and Trimble, W.S. (1999). Phosphatidylinositol polyphosphate binding to the mammalian septin H5 is modulated by GTP. Curr Biol *9*, 1458-1467.

bioRxiv preprint doi: https://doi.org/10.1101/638296; this version posted May 14, 2019. The copyright holder for this preprint (which was not certified by peer review) is the author/funder. All rights reserved. No reuse allowed without permission.

FIGURE LEGENDS

Figure 1. SEPT2/6/7 tunes MT dynamics in a concentration-dependent manner. (a-d) Dot plots show mean (± SEM) rates of MT plus end polymerization (a) and depolymerization (b), and frequency of MT plus end catastrophe (c) and length (d) without SEPT2/6/7 (n = 69) or with SEPT2/6/7 at concentrations of 10 nM (n = 65), 100 nM (n = 51), 200 nM (n = 61), 400 nM (n = 66), 800 nM (n = 50), 1 µM (n = 51), 2 µM (n = 49) and 4 µM (n = 44) of SEPT2/6/7. (e-m) Kymographs show representative microtubule plus end dynamics (red) upon nucleation from MT seeds (green) in the presence of 0 nM (e), 10 nM (f), 100 nM (g), 200 nM (h), 400 nM (i), 800 nM (j), 1 µM (k), 2 µM (l) and 4 µM (m) of SEPT2/6/7. ns: non-significant ($p > 0.05$). *p < 0.05, **p < 0.01, ***p < 0.001, ****p < 0.0001.

Figure 2. SEPT2/6/7 pauses MT plus end growth. (a-c) Kymographs show pausing events during MT growth (b) or shrinkage (c) in the presence of 0 nM (a), 400 nM (b and c, left) and 800 nM (b and c, right) of SEPT2/6/7. (b) Arrowheads point to pause events in the presence of 400 nM and 800 nM of SEPT2/6/7. (c) Arrows point to pause events observed during depolymerization of MT plus ends in the presence of 400 nM and 800 nM of SEPT2/6/7. (d) Images show still frames of MT seeds (green) and dynamic MTs (red) undergoing a pause event during growth in the presence of 800 nM SEPT2/6/7 (d, left) or a pause event during depolymerization in the presence of 400 nM SEPT2/6/7 (d, right). Dashed lines indicate microtubule length during pause events. Time is in min:sec. (e-f) Bar graphs show the percentage of MTs showing continuous growth (no pause, blue) or pause while growing (pause, red) in the presence of 0 nM (n = 69), 10 nM (n = 65), 100 nM (n = 51), 200 nM (n = 61), 400 nM (n = 66), 800 nM (n = 50), 1 µM (n = 51), 2 µM (n = 49) and 4 µM (n = 44) of SEPT2/6/7 or in the presence of 0 nM (n = 21), 10 nM (n = 44), 100 nM (n = 31), 200 nM (n = 38), 400 nM (n = 40) and 800 nM (n = 34) of SEPT9_i1. (g) Bar graphs show the percentage of MTs showing continuous depolymerization (no pause, grey) or pause during shrinkage (pause, orange) in the presence of 0 nM (n = 69), 10 nM (n = 65), 100 nM (n =

bioRxiv preprint doi: https://doi.org/10.1101/638296; this version posted May 14, 2019. The copyright holder for this preprint (which was not certified by peer review) is the author/funder. All rights reserved. No reuse allowed without permission.

51), 200 nM (n = 61), 400 nM (n = 66), 800 nM (n = 50), 1 µM (n = 51), 2 µM (n = 49) and 4 µM (n = 44) of SEPT2/6/7.

Figure 3. SEPT2/6/7 associates with MT lattices and plus end tips. (a) Kymographs show localization of mCherry-SEPT2/6/7 (red) to the lattice of dynamic MT plus end segments and plus end tips (green), and the lattice of GMPCPP MT seeds (magenta, dashed lines). Arrowheads point to mCherry-SEPT2/6/7 localization sites. (b) Bar graph shows the percentage of MTs, which contained mCherry-SEPT2/6/7 (10 nM and 100 nM) only on the lattice of GMPCPP-stabilized MT seeds (magenta), the lattice of dynamic plus ends (green) or plus end tips (orange). In addition, percentage MTs on both seeds and plus end segments (light gray) or on both seeds and plus end tips (dark grey) were quantified. Note that only a very small percentage of MTs showed mCherry-SEPT2/6/7 localization to MT minus ends (red). (c) Kymograph shows an example of mCherry-SEPT2/6/7 (red) tracking the depolymerizing plus end tip (green). Enlargements and arrows show the localization of mCherry-SEPT2/6/7. (d) Kymographs show the localization of mCherry-SEPT2/6/7 (red) at 200 nM, 400 nM and 800 nM to the lattice of GMPCPP MT seeds (magenta or dashed outlines) and the lattice of dynamic MT plus end segments (green). (e) Line scans show the fluorescence intensity changes of mCherry-SEPT2/6/7 (red) along the length of GMPCPP MT seed (magenta) and the MT plus end segment at 200 nM (left), 400 nM (middle) and 800 nM (right) of mCherry-SEPT2/6/7. (f) Dot plots show the mean (± SEM) fluorescence intensity of mCherry-SEPT2/6/7 on GMPCCP-stable seeds and dynamic plus ends (lattice and tips). Quantification was performed from images of MTs after 15 minutes of incubation with 100 nM (n = 29), 200 nM (n = 35), 400 nM (n = 30) and 800 nM (n = 35) of mCherry-SEPT2/6/7. (g) Images show representative examples of the localization of mCherry-SEPT2/6/7 (red) on MT seeds (magenta; dashed outlines) and MT plus end segments (green) at the indicated concentrations. Note that mCherry-SEPT2/6/7 binds to both seeds and plus end segments but

bioRxiv preprint doi: https://doi.org/10.1101/638296; this version posted May 14, 2019. The copyright holder for this preprint (which was not certified by peer review) is the author/funder. All rights reserved. No reuse allowed without permission.

shows stronger preference for MT seeds. ns: non-significant ($p > 0.05$). *p < 0.05, **p < 0.01, ***p < 0.001, ****p < 0.0001.

Figure 4. SEPT2/6/7 inhibits EB1 binding to MT plus ends in a concentration-dependent manner. (a) Kymographs show examples of polymerizing MTs (dim magenta; GMPCCP-stable seeds in bright magenta) with GFP-EB1 (75 nM; green) in the absence or presence of mCherry-SEPT2/6/7 at increasing concentrations (red; 100 - 800 nM). Note that the intensity of GFP-EB1 is decreased with increasing concentrations of mCherry-SEPT2/6/7. (b) Dot plots show the mean (± SEM) fluorescence intensity of GFP-EB1 at MT plus end tips in the absence (n = 28) or presence of 100 nM (n = 22), 200 nM (n = 24), 400 nM (n = 13) and 800 nM (n = 21) of mCherry-SEPT2/6/7. (c) Dot plots show the mean (± SEM) fluorescent intensity of mCherry-SEPT2/6/7 on GMPCPP and GTPγS seeds. Quantification was performed from static images of MTs after 15 min of incubation in the presence of 10 nM (GMPCPP, n = 181; GTPγS, n = 155), 100 nM (GMPCPP, n = 178; GTPγS, n = 139), 200 nM (GMPCPP, n = 186; GTPγS, n = 180), 400 nM (GMPCPP, n = 223; GTPγS, n = 174) and 800 nM (GMPCPP, n = 162; GTPγS, n = 78) of mCherry-SEPT2/6/7. (d) Images show examples of GTPγS seeds (magenta) incubated with 75 nM GFP-EB1 (green) and increasing concentrations of mCherry-SEPT2/6/7 (red; 100 - 800 nM). Note that GFP-EB1 binding decreases with increasing concentrations of mCherry-SEPT2/6/7. (e) Dot plots show the mean (± SEM) fluorescent intensity of GFP-EB1 on GTPγS seeds. Quantification was performed from static images of MTs after 15 minutes of incubation without (n = 215) or with mCherry-SEPT2/6/7 at concentractions of 100 nM (n = 271), 200 nM (n = 238), 400 nM (n = 259) and 800 nM (n = 261). ns: non-significant ($p > 0.05$). *p < 0.05, **p < 0.01, ***p < 0.001, ****p < 0.0001.

Figure 5. MT plus end collisions with SEPT2/6/7 filaments enhance pausing and EB1 dissociation. (a) Kymographs show examples of end-on collisions of growing MT plus ends (green; GMPCPP-stable MT seeds in magenta) with mCherry-SEPT2/6/7 or Rhodamine-labeled

bioRxiv preprint doi: https://doi.org/10.1101/638296; this version posted May 14, 2019. The copyright holder for this preprint (which was not certified by peer review) is the author/funder. All rights reserved. No reuse allowed without permission.

actin filaments (red), which were immobilized on the glass matrix. Arrowheads point to sites where dynamic MTs intersect with mCherry-SEPT2/6/7 or Rhodamine-labeled actin filaments. (b) Bar graph shows the percentage of intersection events in which MT plus ends paused (red) upon encountering SEPT2/6/7 (n = 102 events) or actin filaments (n = 93 events), continued to grow (blue) or depolymerized (green). Note that the percentage of pause events increased by two-fold upon encountering SEPT2/6/7 compared to actin. (c) Kymographs show examples of dynamic MTs (magenta) assembled with 75 nM GFP-EB1 (green) in the presence of immobilized mCherry-SEPT2/6/7 or Rhodamine-labeled actin filaments (red). Arrowheads point to sites where dynamic MTs and GFP-EB1 intersect with mCherry-SEPT2/6/7 and actin filaments. Note that GFP-EB1 binding at the MT plus end tips is reduced or lost at points of intersection with mCherry-SEPT2/6/7 filaments. (d) Bar graph shows the percentage of events at which GFP-EB1 was reduced or lost from MT plus ends (red) or remained unaffected (yellow) upon encountering mCherry-SEPT2/6/7 (n = 107 events) or actin filaments (n = 97 events). (e) Bar graph shows the percentage of events of MT plus ends with GFP-EB1 (75 nM), which paused (red) upon encountering mCherry-SEPT2/6/7 (n = 107 events) or actin filaments (n = 97 events), continued to grow (blue) or depolymerized (green). Note that the percentage of pause events was two-fold more frequent upon encountering SEPT2/6/7 than actin filaments. (f) Kymographs show examples of end-on collisions of EB3 comets (red) with GFP-SEPT7 filaments (green) in rat hippocampal neurons. Arrowheads and enlargements show sites where EB3 comets intersect with GFP-SEPT7 filaments. Note that EB3 intensity is reduced and subsequently disappears upon encountering GFP-SEPT7. (g) Kymograph shows an example of an EB3 comet that disappears upon encountering and pausing at a GFP-SEPT7 filament. Arrowheads and enlargement show a pause site where an EB3 comet intersects and dissappears upon encountering a GFP-SEPT7 filament. Bar graph shows the percentage of pausing events (± SEM) of MTs at sites with (SEPT7 filaments) or without (No SEPT7 filaments) GFP-SEPT7.

bioRxiv preprint doi: https://doi.org/10.1101/638296; this version posted May 14, 2019. The copyright holder for this preprint (which was not certified by peer review) is the author/funder. All rights reserved. No reuse allowed without permission.

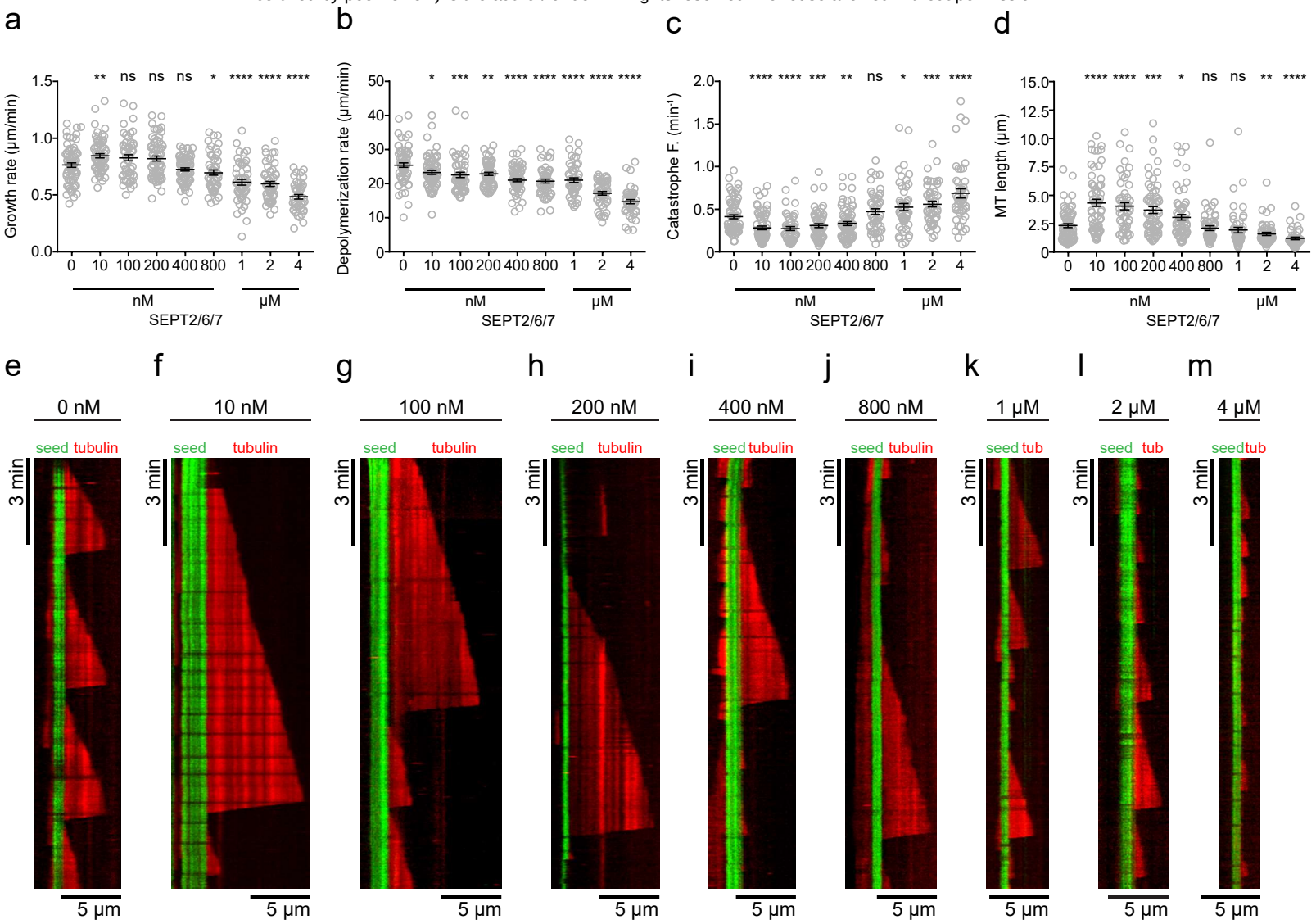

Figure 1 (Nakos et al)

bioRxiv preprint doi: https://doi.org/10.1101/638296; this version posted May 14, 2019. The copyright holder for this preprint (which was not certified by peer review) is the author/funder. All rights reserved. No reuse allowed without permission.

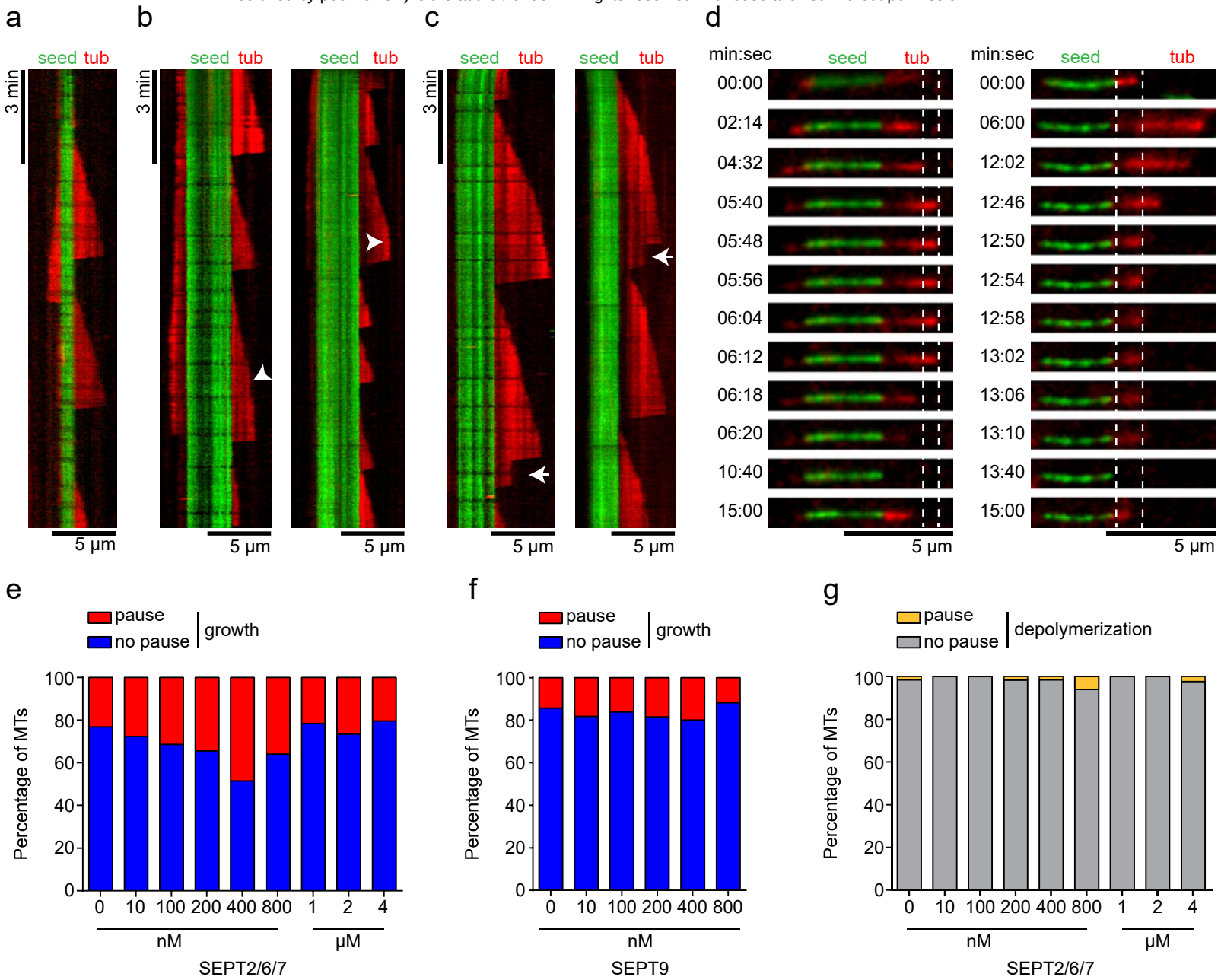

Figure 2 (Nakos et al)

bioRxiv preprint doi: https://doi.org/10.1101/638296; this version posted May 14, 2019. The copyright holder for this preprint (which was not certified by peer review) is the author/funder. All rights reserved. No reuse allowed without permission.

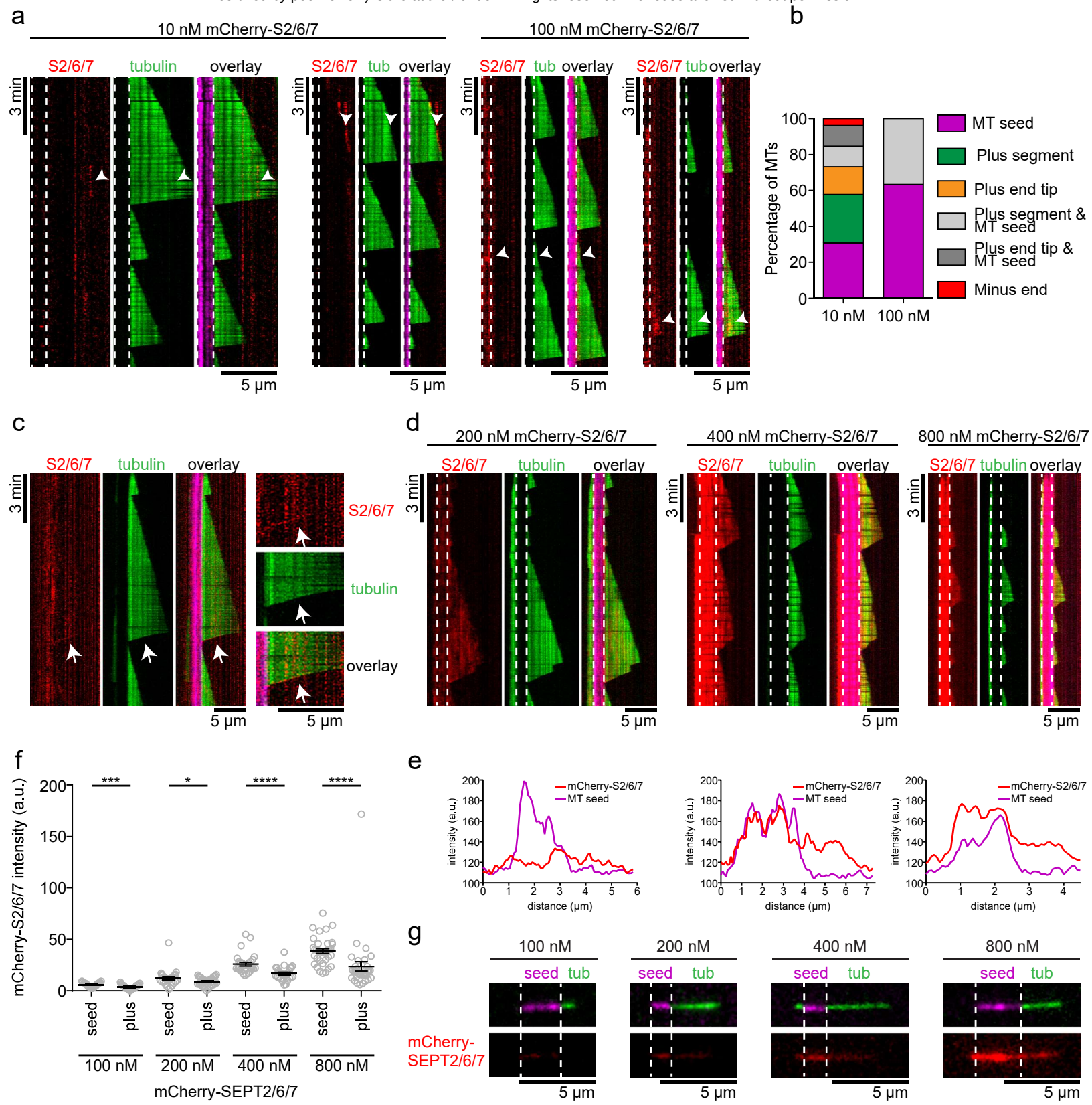

Figure 3 (Nakos et al)

bioRxiv preprint doi: https://doi.org/10.1101/638296; this version posted May 14, 2019. The copyright holder for this preprint (which was not certified by peer review) is the author/funder. All rights reserved. No reuse allowed without permission.

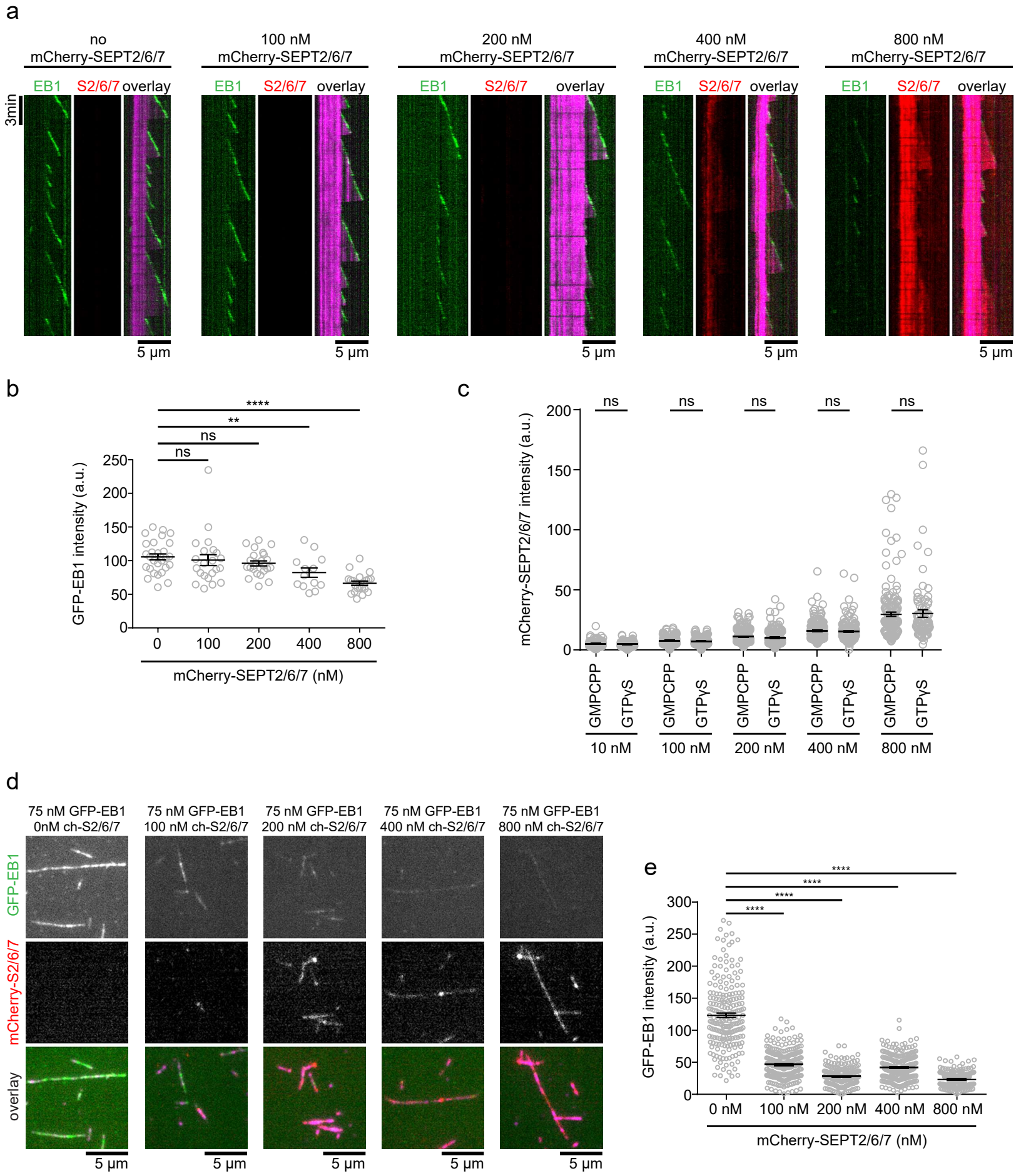

Figure 4 (Nakos et al)

bioRxiv preprint doi: https://doi.org/10.1101/638296; this version posted May 14, 2019. The copyright holder for this preprint (which was not certified by peer review) is the author/funder. All rights reserved. No reuse allowed without permission.

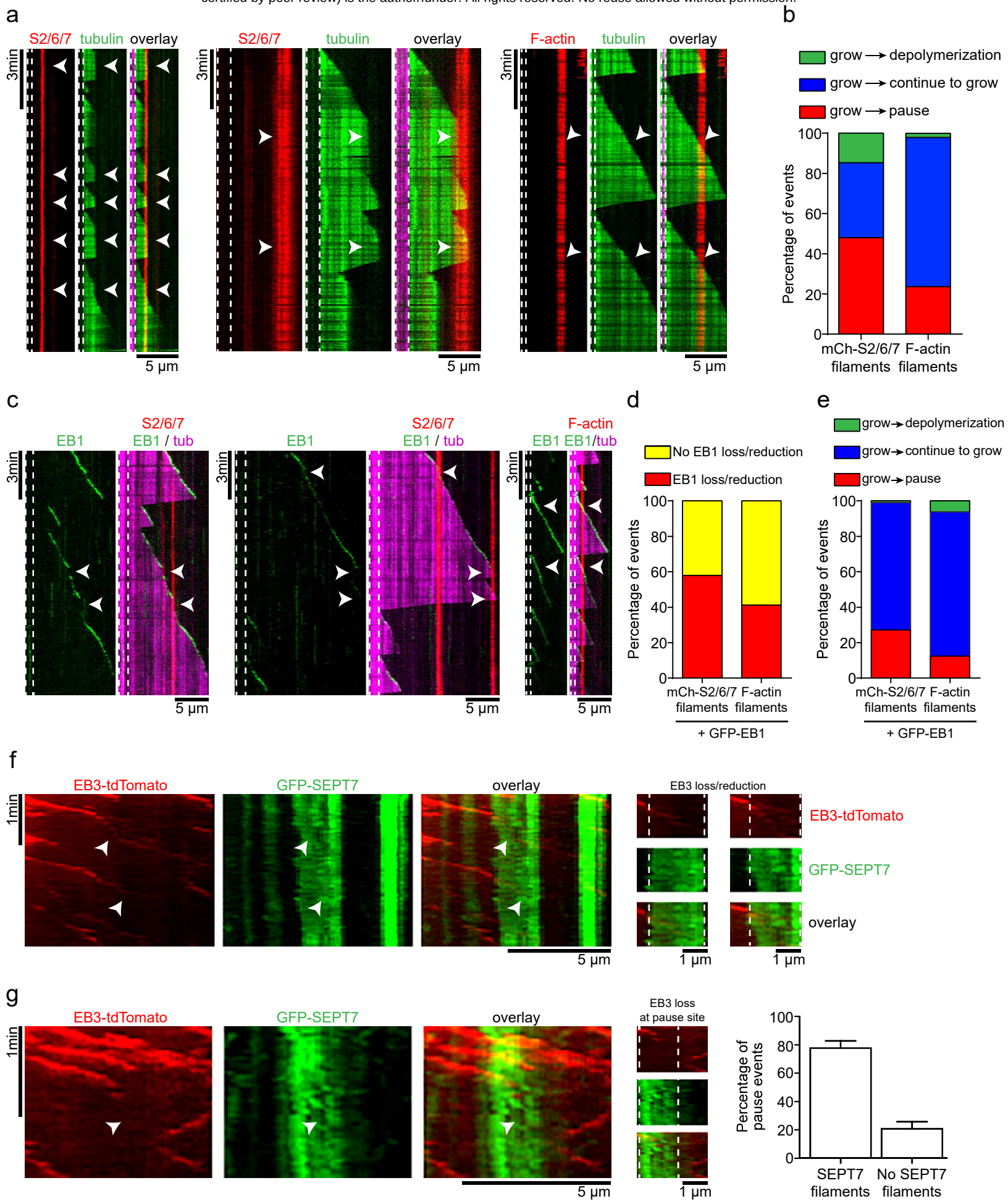

Figure 5 (Nakos et al)